

Inversion workflow for multiphysics modelling of triaxial experiments

Author:

Lin, Jack

Publication Date:

2019

DOI:

<https://doi.org/10.26190/unsworks/21337>

License:

<https://creativecommons.org/licenses/by-nc-nd/3.0/au/>

Link to license to see what you are allowed to do with this resource.

Downloaded from <http://hdl.handle.net/1959.4/63240> in <https://unsworks.unsw.edu.au> on 2024-04-19

THE UNIVERSITY OF NEW SOUTH WALES

SCHOOL OF MINERALS AND
ENERGY RESOURCES ENGINEERING
FACULTY OF ENGINEERING

*Inversion workflow for
multiphysics
modelling of triaxial
experiments*

Jack Lin

A thesis in fulfilment of the requirements for the degree of
Master of Philosophy in Petroleum Engineering

March 2019

Supervisors: Thomas Poulet, Manolis Veveakis

Thesis/Dissertation Sheet

Surname/Family Name	:	LIN
Given Name/s	:	JACK
Abbreviation for degree as give in the University calendar	:	MPhil
Faculty	:	Faculty of Engineering
School	:	School of Minerals and Energy Resources Engineering
Thesis Title	:	Inversion Workflow For Multiphysics Modelling of Triaxial Experiments

Abstract 350 words maximum: (PLEASE TYPE)

As multiphysics geomechanical models are developed, their increasing complexity and number of parameters make it particularly difficult to calibrate against experimental data. In this contribution, I present a heuristic workflow to invert for parameters of a coupled Thermo-Hydro-Mechanical (THM) model in a way that helps the theoretical modellers refine their definition of the underlying elasto-visco-plastic model itself. I apply this workflow to the calibration of deviatoric and volumetric data for two sets of triaxial experiments on mudstone and sandstone. I show that beyond the calibration of well-defined parameters of the THM model, one or two scaling factors of the experimentally obtained yield surface and two more factors to capture the confinement and pore pressure dependency of the flow law lead to the satisfactory matching of two series of six experiments at varying confinements for two different rock types. Using this physical model, I also show that, for the problem of volumetric pore collapse, tracking the volumetric component of the mechanical power in the numerical simulations might allow reducing the number of experiments required to calibrate the model.

Declaration relating to disposition of project thesis/dissertation

I hereby grant to the University of New South Wales or its agents the right to archive and to make available my thesis or dissertation in whole or in part in the University libraries in all forms of media, now or here after known, subject to the provisions of the Copyright Act 1968. I retain all property rights, such as patent rights. I also retain the right to use in future works (such as articles or books) all or part of this thesis or dissertation.

I also authorise University Microfilms to use the 350 word abstract of my thesis in Dissertation Abstracts International (this is applicable to doctoral theses only).

The University recognises that there may be exceptional circumstances requiring restrictions on copying or conditions on use. Requests for restriction for a period of up to 2 years must be made in writing. Requests for a longer period of restriction may be considered in exceptional circumstances and require the approval of the Dean of Graduate Research.

FOR OFFICE USE ONLY Date of completion of requirements for Award:

ORIGINALITY STATEMENT

'I hereby declare that this submission is my own work and to the best of my knowledge it contains no materials previously published or written by another person, or substantial proportions of material which have been accepted for the award of any other degree or diploma at UNSW or any other educational institution, except where due acknowledgement is made in the thesis. Any contribution made to the research by others, with whom I have worked at UNSW or elsewhere, is explicitly acknowledged in the thesis. I also declare that the intellectual content of this thesis is the product of my own work, except to the extent that assistance from others in the project's design and conception or in style, presentation and linguistic expression is acknowledged.'

COPYRIGHT STATEMENT

'I hereby grant the University of New South Wales or its agents the right to archive and to make available my thesis or dissertation in whole or part in the University libraries in all forms of media, now or here after known, subject to the provisions of the Copyright Act 1968. I retain all proprietary rights, such as patent rights. I also retain the right to use in future works (such as articles or books) all or part of this thesis or dissertation.

I also authorise University Microfilms to use the 350 word abstract of my thesis in Dissertation Abstract International (this is applicable to doctoral theses only).

I have either used no substantial portions of copyright material in my thesis or I have obtained permission to use copyright material; where permission has not been granted I have applied/will apply for a partial restriction of the digital copy of my thesis or dissertation.'

AUTHENTICITY STATEMENT

'I certify that the Library deposit digital copy is a direct equivalent of the final officially approved version of my thesis. No emendation of content has occurred and if there are any minor variations in formatting, they are the result of the conversion to digital format.'

INCLUSION OF PUBLICATIONS STATEMENT

UNSW is supportive of candidates publishing their research results during their candidature as detailed in the UNSW Thesis Examination Procedure.

Publications can be used in their thesis in lieu of a Chapter if:

- The student contributed greater than 50% of the content in the publication and is the “primary author”, ie. the student was responsible primarily for the planning, execution and preparation of the work for publication
- The student has approval to include the publication in their thesis in lieu of a Chapter from their supervisor and Postgraduate Coordinator.
- The publication is not subject to any obligations or contractual agreements with a third party that would constrain its inclusion in the thesis

Please indicate whether this thesis contains published material or not.

☐

This thesis contains no publications, either published or submitted for publication (if this box is checked, you may delete all the material on page 2)

☒

Some of the work described in this thesis has been published and it has been documented in the relevant Chapters with acknowledgement (if this box is checked, you may delete all the material on page 2)

☐

This thesis has publications (either published or submitted for publication) incorporated into it in lieu of a chapter and the details are presented below

CANDIDATE'S DECLARATION

I declare that:

- I have complied with the Thesis Examination Procedure
- where I have used a publication in lieu of a Chapter, the listed publication(s) below meet(s) the requirements to be included in the thesis.

Name	Signature	Date (dd/mm/yy)
Jack Lin		

Postgraduate Coordinator's Declaration (to be filled in where publications are used in lieu of Chapters)

I declare that:

- the information below is accurate
- where listed publication(s) have been used in lieu of Chapter(s), their use complies with the Thesis Examination Procedure
- the minimum requirements for the format of the thesis have been met.

PGC's Name	PGC's Signature	Date (dd/mm/yy)

Acknowledgements

A big thank-you to my supervisors, Dr. Thomas Poulet and Dr. Manolis Veveakis, for helping me every step of the way in the last two and a half years, bring me up from absolutely zero knowledge of geomechanics or simulations to where I am now (where I can at least pretend to know what I'm doing).

I would like to acknowledge Dr Sotiris Alevizos, for the many hours of discussions on the finer points of plasticity theory and yield surfaces.

I would like to acknowledge (soon to be) Dr Mustafa Sari, for the many hours of discussions on rocks, how to crush them, how to simulate crushing them, and the myriad ways this could all go wrong.

I would like to acknowledge my family, for putting up with me.

I would like to acknowledge the financial support of my scholarship from the School of Minerals and Energy Resources Engineering at UNSW.

This work was undertaken with the assistance of resources and services from the National Computational Infrastructure (NCI), which is supported by the Australian Government. This work was also supported by resources provided by the Pawsey Supercomputing Centre with funding from the Australian Government and the Government of Western Australia.

Publications arising from this thesis

Portions of this thesis have been published as:

Lin, J., Sari, M., Poulet, T., & Veveakis, M. (2017). An inversion framework for numerical modelling of pore collapse in soft porous rocks. In E. Papamichos, P. Papanastasiou, E. Pasternak, & A. Dyskin (Eds.), *Bifurcation and degradation of geomaterials with engineering applications: Proceedings of the 11th international workshop on bifurcation and degradation in geomaterials dedicated to hans muhlhaus, limassol, cyprus, 21-25 may 2017* (pp. 319–325). Cham: Springer International Publishing. doi: 10.1007/978-3-319-56397-8 40

Portions of this thesis have been submitted as as a journal article as:

Lin, J., Sari, M., Veveakis, M., & Poulet, T. (2019). A heuristic model inversion for coupled thermo-hydro-mechanical modeling of triaxial experiments. ((under review))

Abstract

As multiphysics geomechanical models are developed, their increasing complexity and number of parameters make it particularly difficult to calibrate against experimental data. In this contribution, I present a heuristic workflow to invert for parameters of a coupled Thermo-Hydro-Mechanical (THM) model in a way that helps the theoretical modellers refine their definition of the underlying elasto-visco-plastic model itself. I apply this workflow to the calibration of deviatoric and volumetric data for two sets of triaxial experiments on mudstone and sandstone. I show that beyond the calibration of well-defined parameters of the THM model, one or two scaling factors of the experimentally obtained yield surface and two more factors to capture the confinement and pore pressure dependency of the flow law lead to the satisfactory matching of two series of six experiments at varying confinements for two different rock types. Using this physical model, I also show that, for the problem of volumetric pore collapse, tracking the volumetric component of the mechanical power in the numerical simulations might allow reducing the number of experiments required to calibrate the model.

Contents

1	Introduction	1
2	Forward model	4
2.1	Uncertainties of the geomechanical model	4
2.1.1	Temperature effect	6
2.1.2	Pore pressure effect	7
2.1.3	Rate sensitivity	7
2.1.4	Plasticity model	8
2.2	Numerical implementation	10
2.2.1	Conventions	10
2.2.2	Boundary conditions	10
2.2.3	MOOSE and REDBACK	11
2.2.4	$p' - q$ space	11
2.2.5	Overstress and potential surfaces	12
2.2.6	Mesh sensitivity and localisation	15
3	Inversion workflow	16
3.1	Model parameters	16
3.2	Optimisation algorithm	17
3.3	Objective function	18
3.3.1	Pseudocode for the objective function	21
4	Pathfinder 2.0	22
4.1	Heuristics and automation: a hybrid strategy	22
4.2	Scientific workflows	23
4.3	Meeting requirements	23
4.4	Components of Pathfinder	25
4.4.1	Pre-processing	25
4.4.2	Simulation management	26
4.4.3	Parameter optimization	26
4.4.4	Post-processing	29
5	Case study: Noto diatomaceous mudstone	30
5.1	Rock description	30
5.2	Triaxial experiment description	30
5.3	Simulation and parameter inversion	32

6	Case study: Adamswiller sandstone	39
6.1	Rock description	39
6.2	Triaxial experiment description	39
6.3	Simulation and parameter inversion	42
7	Flow law sensitivity analysis and saddle point	47
7.1	Parameter space	48
7.2	Map of objective functions against experimental data	48
7.3	Correlating simulation response to objective function	49
7.4	Determining the saddle point in α_1 - α_2 space	53
	7.4.1 Second partial derivative test	53
	7.4.2 Numerical approximation	54
8	Discussion and conclusion	56

List of Figures

1.1	Schematic workflows (A) most commonly and (B) in this study.	3
2.1	Schematic representation of two main methods to determine a yield point (circled) from (a) a triaxial experiment or (b) an isotropic compression test, using an exaggerated offset (distance between parallel dashed lines) for illustration purposes.	9
2.2	Numerical model setup. The top and bottom faces are drained and fixed in horizontal displacement. All vertical faces are impermeable and kept at constant temperature. Reproduced from (Poulet & Veveakis, 2016).	11
2.3	Decomposition of the plastic flow rule in volumetric and deviatoric components. Figure reproduced from (Poulet & Veveakis, 2016).	12
2.4	responses with $\gamma_1=1$ (left), $\gamma_1=6$ (right). γ_2 and M are back-calculated so that the tip of the yield surface is at the same point in $p' - q$ space. This results in visually almost identical yield surfaces, but the plastic potential varies significantly.	13
2.5	stress-strain responses for two simulations with identical parameters, using the differing yield surfaces from Fig. 2.4.	14
2.6	Mesh sensitivity analysis showing the deviatoric stress vs. axial strain for simulations of CD1 (Noto mudstone) with different mesh sizes. reproduced from (Sari, 2019).	15
3.1	Schematic description of the optimisation process, broken down in three main steps to optimise sequentially the flow law parameters, yield surface scaling parameters and all other material parameters until global convergence is reached.	19
3.2	Schematic description of the objective function (f) computation, showing its volumetric and deviatoric components for a series of experiments at various confinements. See the full explanation in Sec. 3.3.	20
4.1	Parameter inversion in Pathfinder, reproduced from (Lin et al., 2017).	28
4.2	Grid search on PSO hyperparameters	28
5.1	Physical parameters for triaxial experiments; excerpted from (Oka et al., 2011)	31
5.2	Experiment responses in consolidated-drained CD triaxial tests, excerpted from (Oka et. al, 2011)	33

5.3	Effective stress paths and yield surface in triaxial tests, (Oka et. al, 2011)	35
5.4	Experimentally determined yield points (black circles) for mudstone by Oka et al. (2011) and corresponding yield envelope (thin line), as well as result yield envelope (thick line) obtained from the inversion process, scaling the experimental yield envelope along the Critical State Line (dashed line). The thick lines in light grey show the stress paths for all confined drained experiments CD1-6. The triangles mark yield points obtained from the experimental data at 0.2% plastic strain.	36
5.5	3D mesh used in FEM simulations of Noto mudstone	37
5.6	Deviatoric stress as function of axial strain at various confinements; comparison of numerical (solid lines) and experimental results (dashed lines).	37
5.7	Volumetric strain curves in function of mean effective stress at various confinements for mudstone; comparison of numerical (solid lines) and experimental results (dashed lines).	38
6.1	Stress-strain behaviour in consolidated-drained CD triaxial tests, (T. Wong & Baud, 1999). The solid curves are for samples which failed by shear localization, and the dashed curves are for samples which failed by cataclastic flow, with delocalized compaction and strain hardening.	41
6.2	effective mean stress vs porosity change, reproduced from (Wong et.al, 1997)	42
6.3	Reported yield points in $p' - q$ space	43
6.4	Finite Element mesh used for sandstone simulations	43
6.5	Experimentally determined yield points (black circles) for sandstone by (T.-F. Wong et al., 1997) and corresponding yield envelope (thick line), as well as result yield envelope (thin line) obtained from the inversion process, scaling the experimental yield envelope along the Critical State Line (dashed line) with a shift in pre-consolidation pressure. The thick lines in light grey show the stress paths for all confined drained experiments CD1-6.	44
6.6	Stress strain curves at various confinements for sandstone; comparison of numerical (solid lines) and experimental results (dashed lines). . . .	45
6.7	Volumetric strain curves at various confinements for sandstone; comparison of numerical (solid lines) and experimental results (dashed lines). . . .	45
7.1	Map of the objective function in $\alpha_1 - \alpha_2$ space for CD4-6 of Noto mudstone. Blue color represents region of low cost. Interpolated via radial basis function.	49
7.2	Evolution of the Q_{mech} post-processor and cost function (right) over time, from start of plasticity to end of experiment. The Q_{mech} data is taken from the center block. Blue represents low values, red represents high values, white represents omitted areas.	50

7.3	Evolution of the <i>volumetric_plastic_mechanical_power</i> post-processor (left) and objective function (right) over time, from the start of plasticity to end of experiment. The post-processor data is taken from the center block. Blue represents low values, red represents high values, white represents omitted areas.	50
7.4	Sensitivity analysis in (α_1, α_2) parameter space for mudstone experiments CD4-6. The top row displays the value of the objective function interpolated from 313 simulations (white dots), showing a localised zone of good fits (low values). The bottom row shows the corresponding values of a post-processor computing the volumetric component of the plastic mechanical work at the center of the sample. The red dot shows the location of identified saddle points. Note that some colorbars were capped to exclude extreme values and better illustrate the patterns.	51
7.5	3D plot of the process for finding a saddle point in α_1 - α_2 space, on a synthetic function $h(x, y) = x^2 - y^2$ to illustrate the functionality. Red dots are sampled from $h(x, y)$ with added noise. The light blue surface is the fitted polynomial $f(x, y)$, and the large dark blue dot is the found saddle point. Despite heavy noise, the polynomial tracks the underlying function closely, and the saddle point, found at $[-0.030, -0.008]$, is close to the analytical solution of $[0, 0]$	52
8.1	Sensitivity analysis on Gruntfest number Gr , showing noticeable temperature weakening on the stress-strain curves (left) for corresponding temperature values (right) not exceeding $1^\circ C$ at the centre of the 3D block.	58
8.2	Sensitivity analysis on Arrhenius number Ar , showing extremely different mechanical responses on the stress-strain curves (left) for corresponding temperature values (right) not exceeding $0.2^\circ C$ at the centre of the 3D block.	59

List of Tables

1.1	Non-exhaustive list of sources of uncertainties	3
3.1	List of all parameters to invert for in the numerical simulations of tri-axial experiments	17
5.1	Parameter values obtained for the fits of mudstone experiments shown in Fig. 5.6 and Fig. 5.7.	34
6.1	Parameter values obtained for the fits of sandstone experiments shown in Fig. 6.6 and Fig. 6.7.	46
7.1	Partial List of post-processors in REDBACK. Each post-processor except for <code>top_avg_stress_yy</code> is calculated in three locations: in the centre block, averaged over entire volume, and the extrema (min or max depending on context) of the entire volume.	55

Chapter 1

Introduction

Geomechanics laboratories worldwide perform triaxial experiments on a daily basis, for the purpose of understanding rock behaviours and measuring relevant properties used by diverse theoretical models in academia and various industries. Given the long history of geomechanics, comprehensive experimental results and observations exist nowadays to characterise most rocks around ambient conditions, also providing a fair insight into the corresponding sensitivities with respect to temperature, pore pressure, confinement, or loading rate, just to name a few. The most conventional manner to account for such dependencies has consisted for a long time in approaching geomechanical modelling from a purely mechanical perspective, using traditional constitutive models, and account for the variations of other (secondary) physical processes like temperature and pressure through their influence on the parameters used in the constitutive model (e.g. yield envelope). While successfully providing an empirical way to incorporate more physics in geomechanics, this approach still presents some limitations to tackle situations where feedback couplings between physical processes are too strong, as is the case for the study of material instabilities for example. For those applications, tighter couplings are sought, motivated by the fundamental understanding of the physical processes at play from a multiphysics perspective. The non-mechanical processes are then considered at the same level as the mechanics itself, acknowledging that non-noticeable temperature or pressure changes at the sample scale, during a triaxial experiment, do not prevent temperature or pressure changes at the micro-scale from affecting the overall rock behaviour and localisation in particular, as was shown for mudstone for example (Poulet & Veveakis, 2016). Considering the relative infancy and increased complexity of those multiphysics models, however, begs the question of calibrating the input parameters required to match experimental results.

Inverting for numerical parameters of a theoretical model to match experimental results can be challenging, even for a simple model with a low number of param-

ters, because of the overall uncertainty arising from cumulative errors at all levels: theoretical, experimental and numerical (see Table 1.1).

Uncertainty is probably most intuitively accepted at the experimental level, where physical limitations of the experimental apparatus (precision based on quality), including the measuring equipment, are obvious factors. They are, however, not the only ones. Rocks themselves are naturally inhomogeneous and it is difficult to obtain enough representative samples, as the determination of a Representative Elementary Volume (REV) is a difficult task in itself. Human factors must also be taken into account, regarding the choice and quality of the sampling (accidental damage, contamination), calibration of the machines and other possible mishandling mistakes. Uncertainty at the numerical level is also obvious as rounding errors and risks of hardware failure are well understood. Yet, those effects are probably negligible compared to the risks arising from programmers and operators when selecting the theoretical model, implementing the numerical tools, defining the meshing level, determining the input parameter design (for stochastic generation) or simply inputting data. Uncertainty also arises at the theoretical level itself, due to the need of listing of physical processes considered (under- or over-estimation) and all interactions (known or unknown) between those physical processes, which affect the size of the REV. Modellers can also select unsuitable theoretical models, not necessarily by lack of understanding of all hypotheses behind the models, but also because other physical processes than mechanics can affect those applicability hypotheses in a manner that is simply not yet fully understood. Dealing with this uncertainty led to the active development of inversion methods based on multi-objective optimisation methods (see (Nguyen-Tuan et al., 2016) and citations within), but no single perfect method has been identified yet as there is "no free lunch" - the performance of any two algorithms are equivalent across all possible problems (Wolpert & Macready, 1997). Every benefit from a given approach comes with less interesting consequences, and this inversion problem becomes exponentially more difficult as the number of variables increases, leading to an intractable problem so far for most multiphysics approaches.

Metaheuristics are specifically developed to tackle these inversion problems using mathematical optimisation and computer science techniques, dealing with the uncertainties at the experimental and numerical levels with as little as possible human interaction for scalability purposes. Sometimes, however, operators cannot be completely removed from the process, which needs to be interactive (Wijns et al., 2004). This is the case in particular if one wants to account for uncertainties at the theoretical level and modify the constitutive model used during the optimisation process itself (see Fig. 1.1). This applies in particular for theoretical modellers aiming at developing new multiphysics models and is the focus of this study.

Table 1.1: Non-exhaustive list of sources of uncertainties

Types	Sources of uncertainty	Human factors	Non-human factors
Theoretical	Physical processes considered	Under/over-estimation of processes at play	Complex feedbacks between processes
	Constitutive models	Applicability	Model limitations
Experimental	Material sampling	Sampling choices, sampling quality (damage, contamination)	Natural representativeness
	Experiment apparatus	Calibration, mishandling	Machine quality, precision
	Measuring equipment	Calibration, mishandling	Machine quality, precision
Numerical	simulation setup	Evaluation of theoretical model, mesh coarseness, input parameter design, input errors	-
	Simulator and underlying libraries	Imperfect/incomplete code verification (implementation errors)	rounding errors, hardware failure
	Post-processing	Implementation	rounding errors, hardware failure

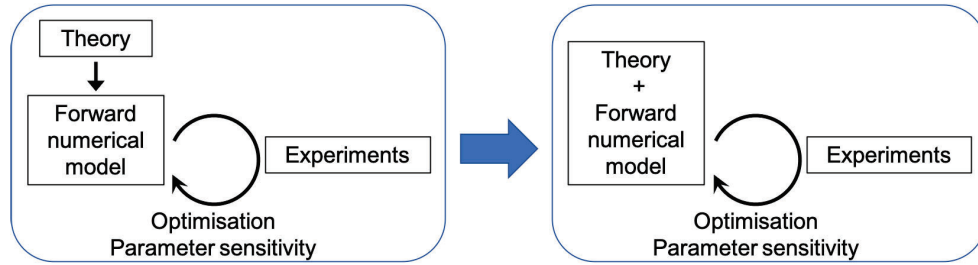


Figure 1.1: Schematic workflows (A) most commonly and (B) in this study.

In this contribution I present a model inversion for coupled Thermo-Hydro-Mechanical (THM) modelling of triaxial experiments, which is heuristic in the literal definition of the term, i.e. enabling the theoretical modellers to learn from the optimisation workflow to refine their multiphysics model. The aim is to extend the work of (Poulet & Veveakis, 2016) and describe the process for capturing the temperature and pressure dependencies of the mechanical enthalpy formulation on which the constitutive model is based. Chapter 2 describes the multiphysics geomechanical model used. Chapter 3 presents the inversion workflow to calibrate the model against experiments. Chapter 4 presents Pathfinder, a suite of tools I developed to automate and facilitate this workflow. Chapters 5 and 6 discuss the application of my workflow to two sets of experiments on mudstone and sandstone. Finally, Chapter 7 discusses the utility of this approach in facilitating theoretical model development, and presents a new, potentially game-changing discovery in the model used.

Chapter 2

Forward model

2.1 Uncertainties of the geomechanical model

The theoretical model at the core of this study is an elasto-visco-plastic model that was specifically developed to investigate material instabilities like pore collapse (Poulet & Veveakis, 2016). The model is based on the traditional momentum, mass and energy conservation equations of a mixture (denoted by the subscript m) composed of a solid matrix (subscript s) fully saturated with fluid (subscript f), along with constitutive equations described in detail in (Poulet & Veveakis, 2016). Neglecting gravity and any chemical reaction and advection terms in the context of quasi-static triaxial experiments, these equations express the evolution of the system as

$$0 = \partial_j \sigma'_{ij} - \partial_i p_f, \quad (2.1a)$$

$$0 = \beta_m \partial_t p_f - \partial_i \left[\frac{\kappa}{\mu_f} \partial_i p_f \right] - \lambda_m \partial_t T + v_{i,i}^{(s)}, \quad (2.1b)$$

$$0 = (\rho C_p)_m \frac{DT}{Dt} - \partial_{ii} T - \chi \sigma_{ij} \dot{\epsilon}_{ij}^{pl}. \quad (2.1c)$$

where σ' represents the effective stress, β the compressibility, λ the thermal expansion coefficient, κ the permeability, μ the viscosity, $v^{(s)}$ the solid velocity, ρ the density, C_p the specific heat, χ the Taylor-Quinney coefficient, and $\dot{\epsilon}^{pl}$ the plastic strain rate.

Following (Poulet & Veveakis, 2016), I introduce the following normalised variables

$$p^* = \frac{p_f}{\sigma_{ref}}, \quad (2.2a)$$

$$T^* = \frac{T - T_{ref}}{T_{ref}}, \quad (2.2b)$$

$$x^* = \frac{x}{x_{ref}}, \quad (2.2c)$$

$$t^* = \frac{c_{th,ref}}{x_{ref}^2} t, \quad (2.2d)$$

where σ_{ref} , T_{ref} , x_{ref} and $c_{th,ref}$ are reference values for the stress, temperature, length and thermal diffusivity of the mixture respectively. Using all normalised variables and dropping the asterisk notation for simplicity, I work in this study with the following system of equations expressing the evolution of the temperature (T), pore fluid pressure (p_f) and displacement (u_i , $1 \leq i \leq 3$) as

$$0 = \partial_j \sigma'_{ij} - \partial_i p_f, \quad (2.3a)$$

$$0 = \partial_t p_f - \partial_i \left[\frac{1}{Le} \partial_i p_f \right] - \Lambda \partial_t T + \frac{Pe \dot{\epsilon}_V}{\beta_m}, \quad (2.3b)$$

$$0 = \partial_t T - \partial_{ii} T - Gr \sigma_{ij} \dot{\epsilon}_{ij}^p. \quad (2.3c)$$

This formulation uses dimensionless groups including the Lewis number Le , Gruntfest number Gr and thermal pressurisation Λ defined as

$$Le = \frac{\mu_f c_{th,ref} \beta_m}{\kappa} \quad (2.4a)$$

$$Gr = \frac{\sigma_{ref}}{T_{ref}(\rho C_p)_m} \chi, \quad (2.4b)$$

$$\Lambda = \frac{\lambda_m \delta T_{ref}}{\beta_m \sigma_{ref}}. \quad (2.4c)$$

To derive material properties for the samples, This formulation uses fairly simple mixture rules for combining the physical properties of fluid (f) and solid (s) into an overall mixture property using the porosity ϕ . Properties derived this way includes the mixture compressibility β_m , mixture thermal expansion λ_m , and mixture thermal conductivity α_m :

$$\beta_m = (1 - \phi)\beta_s + \phi\beta_f \quad (2.5)$$

$$\lambda_m = (1 - \phi)\lambda_s + \phi\lambda_f \quad (2.6)$$

$$\alpha_m = (1 - \phi)\alpha_s + \phi\alpha_f \quad (2.7)$$

The main particularity of this model, built on the overstress plasticity framework of Perzyna (1966) extended by Poulet & Veveakis (2016), is that dependencies on other state variables, such as the confining pressure, excess pore pressure, and thermal effects, are expressed through the definition of the mechanical enthalpy rather than more traditional expressions like the yield envelope and hardening modulus. The intent is to capture the temperature and pressure dependencies of the constitutive model with a physical description (see Sari, 2019), which is a worthy goal but also introduces more uncertainty in terms of model calibration compared to more engineering approaches.

For instance, in many models the evolution of the hardening modulus is an input of the model, defined as a function of strain, and can therefore be monitored rather accurately in the lab and entered directly in simulation to reproduce numerically those laboratory results. This approach can produce very accurate fits to existing data, but sacrifices some of the explaining and predictive power. Instead, the hardening or softening behaviour of the model used in this work can only be altered by changing the values of material parameters, which will in turn impact the stress response, including through variations of temperature or pore pressure, or by modifying the plastic flow law itself (Poulet & Veveakis, 2016) through the definition of the mechanical enthalpy Q_{mech} , or its normalised Arrhenius variable $Ar = \frac{Q_{mech}}{RT_0}$, with R the ideal gas constant, and \tilde{T}_0 the temperature in Kelvin. The associated flow law used is:

$$\dot{\epsilon}_{ij}^{vp} = \dot{\epsilon}_0 \bar{\sigma}^m \exp^{\frac{ArT}{1+T}} \frac{\partial g}{\partial \sigma_{ij}} \quad (2.8)$$

where $\dot{\epsilon}_{ij}^{vp}$ denotes the visco-plastic strain rate, $\dot{\epsilon}_0$ a pre-exponential factor, $\bar{\sigma}$ the overstress, m a material parameter, g the plastic flow potential and R the ideal gas constant.

In this approach, particular attention is paid to the temperature and pore pressure evolutions, which might appear puzzling at first sight when modelling experiments on rocks under isothermal conditions.

2.1.1 Temperature effect

Most triaxial tests are performed under isothermal conditions (often room temperature), which would make it a fair assumption to neglect the temperature effects when modelling the corresponding experiments. The temperature, however, does vary internally due to all dissipative processes taking place at the micro-scale and the temperature increase becomes clearly evident with infra-red radiation (IRR) imaging when a fracture occurs (Wu et al., 2006). While such changes can be accurately monitored with IRR cameras at the precise (and short-lived) moment when a rock sample breaks,

which even allows to monitor temperature as a precursor for rock fracturing and failure (Wu et al., 2006), the external temperature monitoring of a triaxial experiment will unfortunately reveal no evolution until localisation is well pronounced. Indeed, most thermal imaging cameras are usually sensitive to gradations of 0.05-0.15 degrees Celsius, which is not precise enough to detect micro heat signature events, especially if not located on the outside of the sample. The temperature itself, though, is undeniably increasing through dissipation and its effects on the yield stress for instance are well captured by Eyring plots (e.g. Poulet & Veveakis, 2016). Therefore, temperature is considered a primary variable in the current framework, where its evolution is mainly constrained through the values of the Gruntfest number (Gr). Its effect on the mechanics is controlled by the Arrhenius number (Ar).

2.1.2 Pore pressure effect

Similarly to temperature, pore fluid pressure can also play a considerable role at the microstructural level, even in cases where its overall value at the sample level seems rather constant. The normalised mass balance equation (Eq. 2.3b) shows the impact of the Lewis number (Le), expressing the ratio of thermal over mass diffusivities. It accounts therefore not only for the preponderant effect of fluid permeability, but also for any other internal mass diffusion process, including those resulting from physical processes occurring at the micro-scale like pore collapse (Sari, 2019). As such, pore pressure is also tracked as a primary variable, whose value is strongly affected by the Lewis number Le , thermal pressurisation coefficient Λ and compressibility $\bar{\beta}$. Its variation affects the effective stress directly, by definition, and less directly through the pressure dependency of the mechanical dissipation. Those effects impact, in turn, on the temperature through the mechanical dissipation.

2.1.3 Rate sensitivity

The rate sensitivity of geomaterials is another well accepted phenomenon (e.g. Poulet & Veveakis, 2016), which plays an important role when modelling rocks at geological time scales. While considerable efforts are being spent in measuring flow laws from experiments for as many materials as possible under various conditions, as well as developing theoretical models to capture those dependencies (e.g. Mielke, 2006), no consensus exists yet and the problem remains an active research area. Unsurprisingly, the difficulty lies in capturing simultaneously the various cross-dependencies between temperature, pressure and rate. For instance, recent observations showed the increased rate-dependency of calcarenite with compression (Sari, 2019).

2.1.4 Plasticity model

Those sensitivities to temperature, pressure and rate can be captured at various levels in the geomechanical model, which contains itself some inherent uncertainty as many of its constituents are being investigated in the quest for an improved modelling approach.

Activation enthalpy

The main characteristic of the geomechanical approach in this work is the explicit formulation of the mechanical enthalpy Q_{mech} . While the formula initially proposed (Poulet & Veveakis, 2016) remains a guideline, its exact definition is the subject of ongoing research (Sari, 2019) and needs therefore to be considered itself as a free set of parameters in the overall inversion approach of experimental results. Theoretical considerations can provide some constraints on the enthalpy definition (Sari, 2019), but no definitive form has been universally accepted yet. In this contribution, I account therefore for the related uncertainty by taking the definition (Poulet & Veveakis, 2016)

$$Q_{mech} = \alpha_1 + \alpha_2 p_f, \quad (2.9)$$

where α_1 and α_2 are material parameters to be inverted for specific experiments, and p_f is the excess pore pressure.

Yield envelope

Another distinctive aspect of the model used is the definition of the yield surface itself, which differs from the one taken by most traditional geomechanics models. The only available data regarding the yield surface obviously comes from experimental curves, which exhibit characteristic points that can be interpreted as yield points. Both on stress-strain curves from triaxial experiments and isotropic compression tests, an initial straight line is usually interpreted as a linear elastic response, which allows the identification of a yield point as the point on the curve where an arbitrarily determined deviation from that linear elastic response occurs (see Fig. 2.1). It is important to note the two major problems with this determination method, on top of the obvious uncertainty stemming from the experimental results themselves.

Firstly, a yield point can only be determined, by definition, using data from unloading experiments. The initial linear trend of experimental curves does indeed not always correspond to an elastic behaviour, as was shown for the case of calcarenite for instance (Sari, 2019). In that example, even the first unloading sequences during this initial (loading) linear response (which would intuitively be interpreted by many as an elastic regime) showed that the rock had reached plasticity from the very begin-

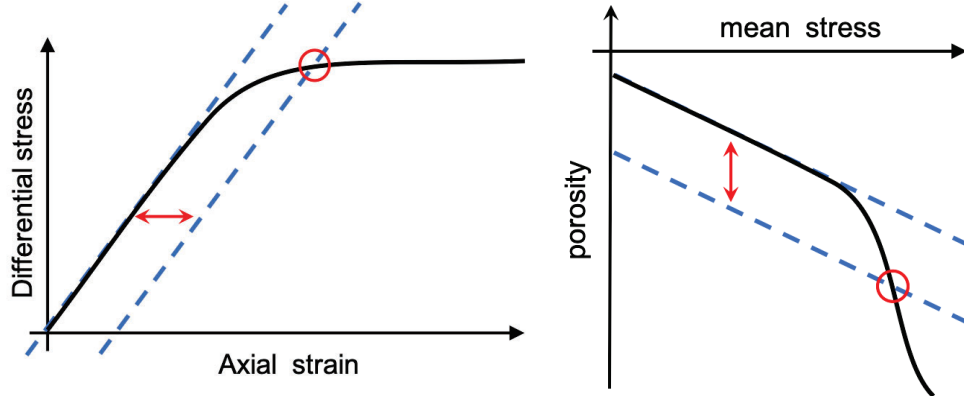


Figure 2.1: Schematic representation of two main methods to determine a yield point (circled) from (a) a triaxial experiment or (b) an isotropic compression test, using an exaggerated offset (distance between parallel dashed lines) for illustration purposes.

ning. Such complex responses raise questions about the existence of a yield envelope altogether.

Secondly, the notion of *yield* can represent different concepts. For instance, the McGraw-Hill Dictionary of Scientific and Technical Terms (Parker, 2003), uses distinctive terms to differentiate those notions they name *yield*, *yield point* and *yield strength*. They define the *yield* as "the stress in a material at which plastic deformation occurs", the *yield point* as "the lowest stress at which strain increases without increase in stress" and the *yield strength* as "the stress in a material at which plastic deformation occurs". Following their terminology, one can see clearly that the *yield strength* is the notion determined experimentally, while the *yield* is the one required for numerical simulations. Naturally, the *yield* must be reached before the *yield strength*, which implies that the yield envelope needed for the simulations can only be smaller than the experimentally obtained one. In this work, I consider the two to differ only by a scaling function, which is taken into account as extra parameters to invert for.

In this contribution, I use a capped model which is well adapted to the two case studies presented in Chapters 5 and 6. This model is an extended version of the Modified Cam-Clay model (Gerolymatou, 2017) which proposes a yield surface defined as

$$q^2 + M^2 h(p)(p - p_t)(p - p_c) = 0 \quad (2.10)$$

where p denotes the mean effective stress, q the deviatoric stress, M the slope of the critical state line, p_c the pre-consolidation pressure and p_t the tension cut-off. A dependence on mean pressure is expressed through the function

$$h(p) = \exp \left[-\frac{1}{\gamma_1} \left(\frac{p - p_t}{p_c - p_t} - \gamma_2 \right)^2 \right] \quad (2.11)$$

where γ_1 and γ_2 are numerical parameters affecting the shape and skewness of the yield surface. Note that this yield surface can lose convexity for certain values of the parameters and needs to be used with care. This definition provides a more flexible yield envelope than the Modified Cam-Clay model, with the ability to break the symmetry by shifting the top point of the envelope.

To constrain the determination of the yield envelope and minimise the number of free parameters, a first envelope is determined by matching the reported experimental data, providing values for all parameters M , p_c , p_t , γ_1 and γ_2 .

A maximum of two degrees of freedom is used to identify the best yield envelope as a transformation of the experimental curve, determined by a new pre-consolidation pressure \tilde{p}_c and new maximum value of deviatoric stress \tilde{q}_{max} , scaling the initial envelope along the Critical State Line joining the tension cut-off with the peak of the envelope of coordinates (p_{max}, q_{max}) in $(p'-q)$ space, as defined in Subsec. 2.2.5. The corresponding value of the mean effective stress \tilde{p}_{max} is therefore defined as

$$\tilde{p}_{max} = p_t + \frac{\tilde{q}_{max}}{q_{max}}(p_{max} - p_t) \quad (2.12)$$

By algebraic manipulation of eq. 2.10, 2.11 and 2.12, a scaled version of the envelope can then be obtained with modified values $\tilde{\gamma}_2$ and \tilde{M} defined as

$$\tilde{\gamma}_2 = 2 \left(\frac{\tilde{p}_{max} - p_t}{\tilde{p}_c - p_t} - \gamma_1 \right) \frac{(\tilde{p}_{max} - p_t)(\tilde{p}_c - \tilde{p}_{max})}{(\tilde{p}_c - p_t)(\tilde{p}_c + p_t - 2\tilde{p}_{max})} \quad (2.13)$$

$$\tilde{M} = \tilde{q}_{max} \exp \left[\frac{1}{2\tilde{\gamma}_2} \left(\frac{\tilde{p}_{max} - p_t}{\tilde{p}_c - p_t} - \gamma_1 \right)^2 \right] \frac{1}{\sqrt{(\tilde{p}_{max} - p_t)(\tilde{p}_c - \tilde{p}_{max})}} \quad (2.14)$$

2.2 Numerical implementation

2.2.1 Conventions

In this work, I assume stresses are taken positive in compression and pore pressure is positive ($p_f > 0$). Index notation is used. The indices used are i,j,k,l. All other letters or character strings appearing as indices belong to the symbol used and are not subject to the index notation rules. Equations assumes a biphasic material, namely a solid and a fluid phase irrespective of the processes involved.

2.2.2 Boundary conditions

The boundary conditions for the simulations in this work follows the setup used in (Poulet & Veveakis, 2016) and simulates a standard confined drained experiment with constant temperature and no-flow imposed as boundary conditions on the sides of the 3D block (see Fig. 2.2). The top and bottom of the samples are drained. A cubic or

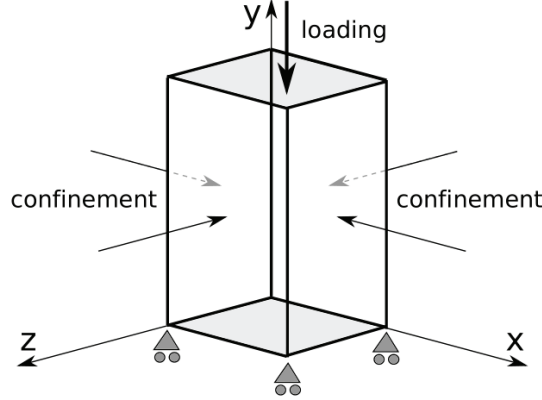


Figure 2.2: Numerical model setup. The top and bottom faces are drained and fixed in horizontal displacement. All vertical faces are impermeable and kept at constant temperature. Reproduced from (Poulet & Veveakis, 2016).

cylindrical mesh can be used to represent the sample, depending on the experiment conditions.

The simulation has two stages. In the initialization stage, the material is equilibrated to a set confining pressure. The bottom face is allowed to move freely in the X and Z directions, while other surfaces are fixed to avoid rotation. When the material is equilibrated, the main simulation starts. In the main simulation, the X and Z displacements of the top and bottom face are fixed at the initialized values. The bottom face is also fixed in the Z direction. A velocity boundary condition is imposed on the top to simulate constant compression. The sides are kept under constant confining pressure.

2.2.3 MOOSE and REDBACK

The numerical implementation of this system of equations is done in REDBACK (Poulet & Veveakis, 2016), an open-source simulator built using the MOOSE framework (Gaston et al., 2009) and its Tensor Mechanics module in particular. MOOSE is used for its capacity to solve tightly coupled systems in parallel, and REDBACK implements all equations presented above using a rate-dependent overstress plasticity framework.

2.2.4 $p' - q$ space

The geomechanical model implemented in REDBACK naturally differentiates the volumetric and deviatoric component of stress (see Fig. 2.3). All calculations for overstress

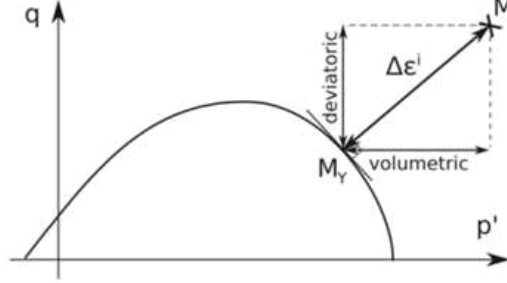


Figure 2.3: Decomposition of the plastic flow rule in volumetric and deviatoric components. Figure reproduced from (Poulet & Veveakis, 2016).

are then performed in the $p' - q$ space, where p' denotes the effective volumetric stress, with the notion of effective stress σ'_{ij} following Terzaghi's principle $\sigma_{ij} = \sigma'_{ij} - p_f \delta_{ij}$. The symbol q denotes the deviatoric stress. The $p' - q$ space is of particular interest as it represents a natural choice to define the yield surface, marking the limit of elasticity, in a study focuses on the volumetric and deviatoric behaviours of rocks.

2.2.5 Overstress and potential surfaces

The definition of the overstress itself is subject to interpretation and modellers have the freedom to propose different descriptions, which all affect modelling results in a fundamental manner. In particular, some algorithmic considerations can be taken into account to define a numerically efficient overstress definition, leading to different methods to compute an overstress measure between a stress point in the plasticity region and its corresponding yield point in the $(p' - q)$ space. In particular, the respective weights of the volumetric and deviatoric components of the overstress play a critical role and justifies the simplest definition proposed in (Poulet et al., 2017).

In (Poulet & Veveakis, 2016), the flow law is defined as:

$$\dot{\epsilon}_{ij}^p = \dot{\lambda} \frac{\partial f}{\partial \sigma_{ij}} \quad (2.15)$$

With f the plastic potential (taken as the yield function in this associated model), $\dot{\lambda}$ the plastic multiplier, dependent on Q_{mech} , defined as:

$$\dot{\lambda} = \sqrt{\left\langle \frac{q - q_Y}{\sigma_{ref}} \right\rangle^{2m} + \left\langle \frac{p - p_Y}{\sigma_{ref}} \right\rangle^{2m}} \exp \left[\frac{-Q_{mech}}{RT} \right] \quad (2.16)$$

Where $\langle . \rangle$ denotes Macaulay brackets; p, q, p_Y, q_Y are the coordinates of a point M and its corresponding yield point M_Y (from Fig. 2.3) respectively. The overstress

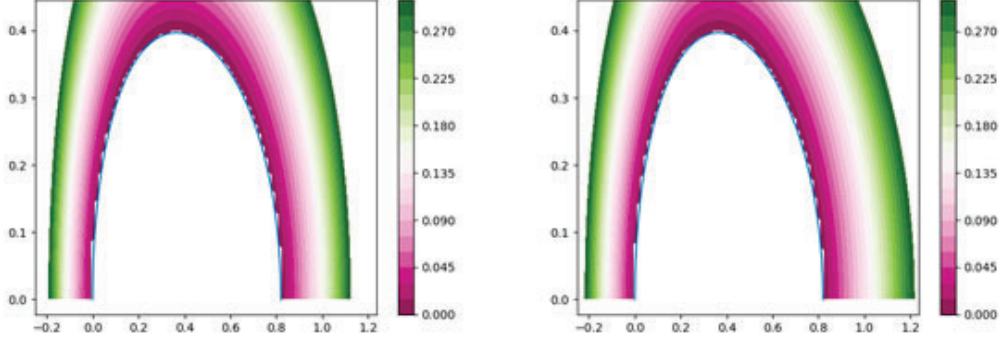


Figure 2.4: responses with $\gamma_1=1$ (left), $\gamma_1=6$ (right). γ_2 and M are back-calculated so that the tip of the yield surface is at the same point in $p' - q$ space. This results in visually almost identical yield surfaces, but the plastic potential varies significantly.

$\sigma_o = \sqrt{\langle \frac{q-q_Y}{\sigma_{ref}} \rangle^{2m} + \langle \frac{p-p_Y}{\sigma_{ref}} \rangle^{2m}}$ represents a simple straight-line distance between M and M_Y .

This method is straightforward and numerically robust. However, considering an associative flow law, it is more conventional to follow the steepest descent of the plastic potential, which leads to slightly different overstress values. A modified Cam Clay surface with this overstress definition was tested as part of this work. While this second definition works well for the simple ellipse of the modified Cam Clay surface, it was found to require very high numerical precision in the overstress calculation, and created convergence problems in the extended mCC surface. For the current implementation of the extended mCC surface used in this work, a third definition is selected with the overstress taken as the square-root of the plastic potential:

$$\sigma_o = \sqrt{q^2 + M_f^2 h(p - p_t)(p - p_c)} \quad (2.17)$$

While simplifying the numerical problem, this third definition creates some interesting consequences of its own. For two yield surfaces that are visually very similar, but having different values for the shape parameters M , γ_1 and γ_2 , the shape of the potential surfaces can differ significantly.

An example is shown in Fig. 2.4, showing two visually identical yield surfaces in $p' - q$ space, but with different growth of potential surfaces. Fig. 2.5 shows two sets of stress-strain curves, using same parameters other than the yield surface. Having quicker-growing potentials naturally leads to more hardening in the response, in a manner roughly analogous to increasing α_2 .

For fitting the experiments in this work, values are chosen so that the ratio between height and width in the yield surface is preserved in the potential surfaces.

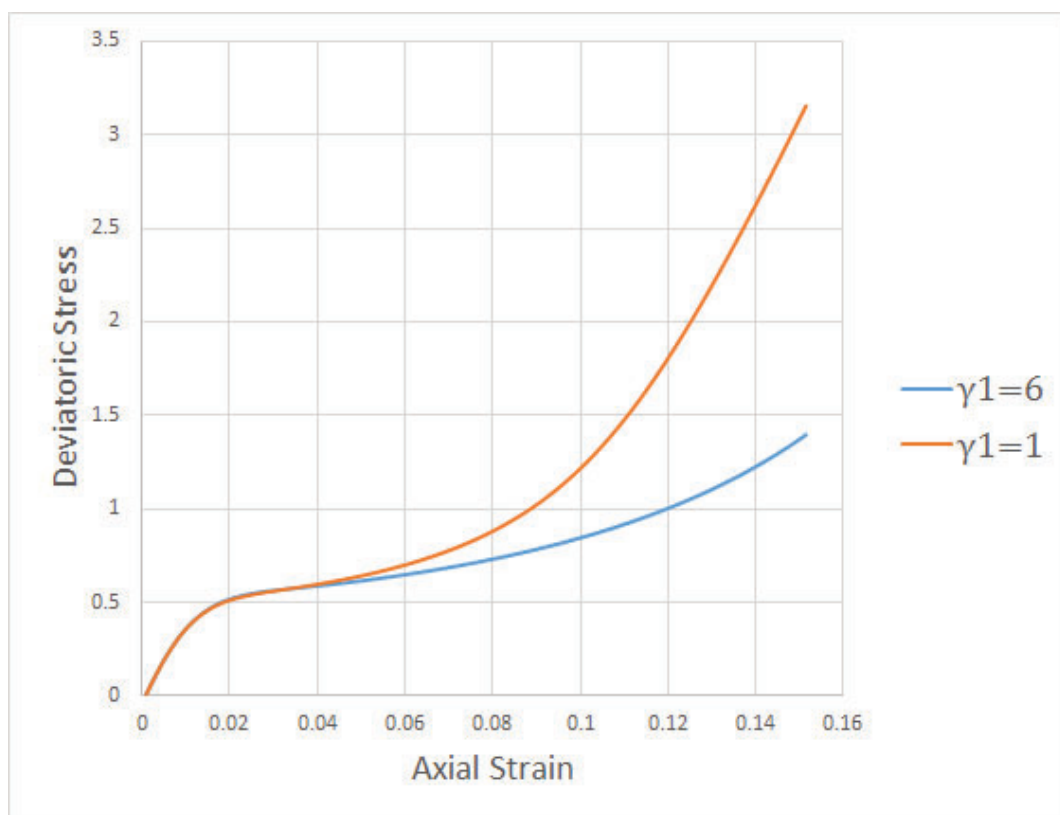


Figure 2.5: stress-strain responses for two simulations with identical parameters, using the differing yield surfaces from Fig. 2.4.

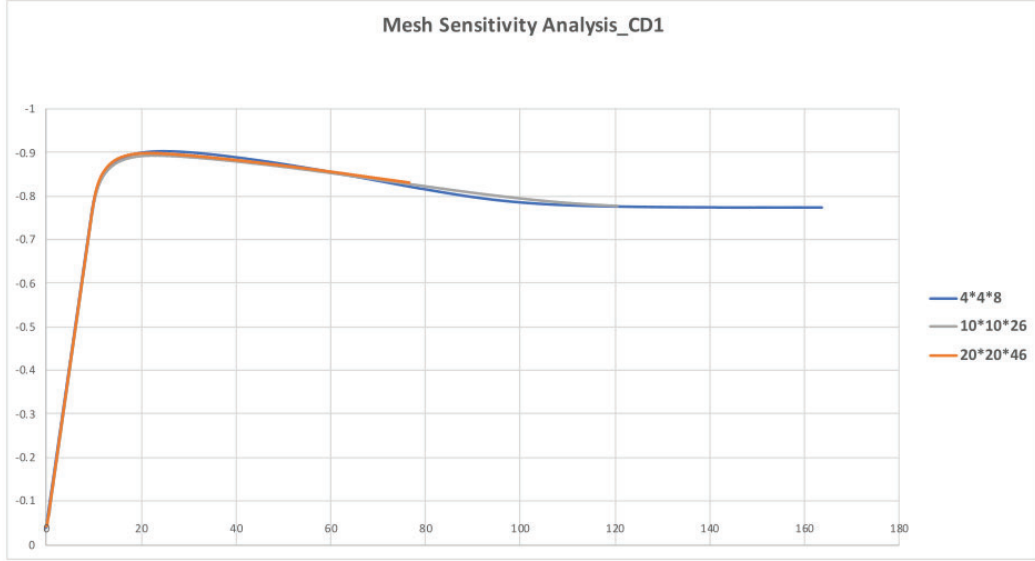


Figure 2.6: Mesh sensitivity analysis showing the deviatoric stress vs. axial strain for simulations of CD1 (Noto mudstone) with different mesh sizes. reproduced from (Sari, 2019).

2.2.6 Mesh sensitivity and localisation

Traditional FEM approaches suffer from mesh sensitivity, i.e. the simulation responses differ depending on the resolution of the finite element mesh. This is particularly the case in strain-weakening regimes. Using the same numerical model and parameters as this work, Sari et al. (2019) ran repeated simulations of strain-weakening mudstone CD1 (see Chapter 5) while varying the mesh size from 128 cells to 18400 cells. The results shown in Fig. 2.6 show little variation in the simulation response.

(Sari et al., 2019) concludes that the introduction of the energy balance equation regularizes the problem of localization of plastic deformation during mechanical softening, providing an internal length and a characteristic time of propagation of the shear band, unlike most traditional solid mechanics approaches. Note that localization occurs (as would be expected from the physical experiments) despite treating all rock samples as homogeneous and using the same material parameters across the entire mesh. A detailed treatment of strain localization can be found in (Poulet & Veveakis, 2016).

Chapter 3

Inversion workflow

This chapter focuses on the inverse problem of identify all parameters needed to match numerical simulations of confined drained triaxial experiments with experimental data. As the longer term goal is to investigate the underlying multiphysical processes involved, the implementation consider all samples to be homogeneous and attribute a single value for each of the material parameters, rather than try to improve the match by introducing spatial distributions for different samples.

Considering the "no-free-lunch theorem" (Wolpert & Macready, 1997), no inversion strategy performs better than all others in all cases. Instead, the optimal algorithm depends on the problem being solved, and I have developed a customized approach tailored to the current model.

3.1 Model parameters

From all considerations presented in Sec. 2.1, a list of parameters to be inverted for can be established (see Table. 3.1), including the material parameters, but also the constitutive models parameters. In particular, as mentioned above, A maximum of two free parameters is used to rescale the yield envelope, and I also invert for the two parameters α_1 and α_2 of the mechanical enthalpy. Most parameters represent usual material properties and can be constrained in reasonably tight ranges from literature and experimental data. A few parameters, including the Lewis number Le , Gruntfest number Gr , and mechanical enthalpy parameters α_1 and α_2 are more poorly constrained.

Parameter name	Symbol	Unit of Measure
Flow law overstress exponent	m	-
Initial permeability	κ	m^2
Initial porosity	ϕ	-
Arrhenius coefficient	Ar	-
Young's modulus	E	Pa
Poisson ratio	ν	-
Fluid thermal diffusivity	$c_{th,f}$	$m^2.s^{-1}$
Fluid thermal expansion coefficient	λ_f	K^{-1}
Fluid viscosity	μ, f	$Pa.s$
Fluid compressibility	β_f	Pa^{-1}
Solid thermal diffusivity	$c_{th,s}$	$m^2.s^{-1}$
Solid thermal expansion coefficient	λ_s	K^{-1}
Solid compressibility	β_m	Pa^{-1}
Mixture thermal diffusivity	$c_{th,m}$	$m^2.s^{-1}$
Mixture thermal expansion coefficient	λ_s	K^{-1}
Mixture compressibility	β_m	Pa^{-1}
Mixture thermal pressurisation coefficient	Λ_m	-
Lewis number	Le	-
Gruntfest number	Gr	-
Yield envelope, pre-consolidation pressure	\tilde{p}_c	Pa
Yield envelope, maximum deviatoric stress	\tilde{q}_{max}	Pa
Mechanical enthalpy parameter α_1	α_1	-
Mechanical enthalpy parameter α_2	α_2	-

Table 3.1: List of all parameters to invert for in the numerical simulations of triaxial experiments

3.2 Optimisation algorithm

Numerous meta-heuristic approaches have been previously developed to invert model parameters from experimental data in geomechanics, and following (Nguyen-Tuan et al., 2016) I am using a Particle Swarm Optimisation (PSO) computational paradigm to perform this task, as it is particularly well suited to investigate optimisation problems with multiple local minima as faced in a multiphysics context. This optimization process is implemented via Pathfinder (covered in Chapter 4), a software suite specifically

developed to orchestrate parameter inversion tasks on the various high-performance computational facilities available.

In order to reduce the computational time and maximise the learning benefit from the optimisation process, not all parameters are inverted for at once, instead the process is broken down in several stages. The inversion process starts by selecting numerical values for all parameters, including reference values for normalisation, as best estimates based on reported values from the experiment, literature values for the rock involved, and previous studies. This provides a starting point from which the parameter optimisation can proceed, following three steps (illustrated in Fig. 3.1). The first step consists in using Pathfinder (see Chapter 4) to optimise the numerical values of α_1 and α_2 for each of the confinement cases individually. As a second step, the scaling parameter of the yield envelope is then optimised manually. The third step sees the adjustment of all other variables, manually or using Pathfinder. In practise, this involves mainly the three variables identified as playing the most important roles: the thermal pressurisation coefficient Λ , Gruntfest number (Gr) and Lewis number (Le). These three steps are repeated iteratively until satisfactory overall convergence is obtained.

3.3 Objective function

Given a series of N confined drained experiments CD_i with $1 \leq i \leq N$ at various confinement pressures, an automatic parameter inversion can be performed through a minimisation of an objective function f , which is taking into account both the volumetric and deviatoric components of the experimental and simulation data to reflect the importance of those two components in the model formulation (see Poulet & Veveakis, 2016). Fig. 3.2 is a graphical representation of the computation.

For each experiment i , the deviatoric component f_i^d of the objective function is expressed as the L2-norm of the difference between the experimental and numerical simulation results of the strain-stress curve for that experiment. Similarly, the volumetric component f_i^v represents the L2-norm of the error on the porosity evolution as a function of strain.

To increase the focus on the impact of the constitutive model in plasticity, both definitions are taken on a subset of the whole range of strain values, from a manually selected value of strain after all experiments display a plastic behaviour until the end of the experiments (horizontal range in between dashed vertical lines on Fig. 3.2). In other words, I am more interested in the plastic behaviour at large strain than on the elastic regime or its transition to the plastic regime.

The overall deviatoric and volumetric objective functions, f^d and f^v , are taken

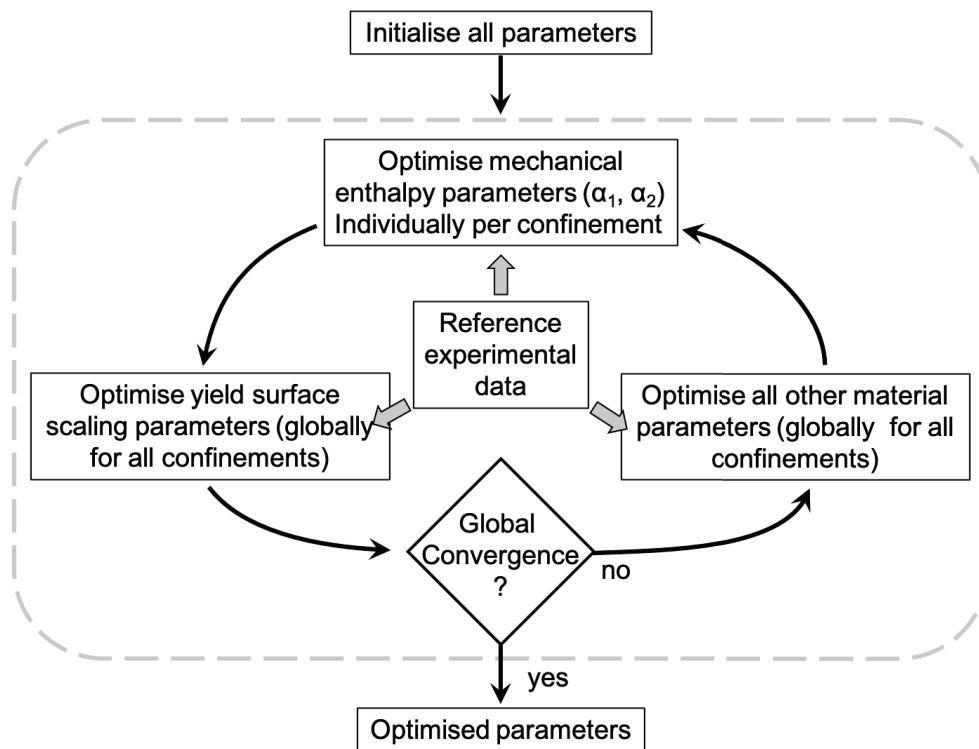


Figure 3.1: Schematic description of the optimisation process, broken down in three main steps to optimise sequentially the flow law parameters, yield surface scaling parameters and all other material parameters until global convergence is reached.

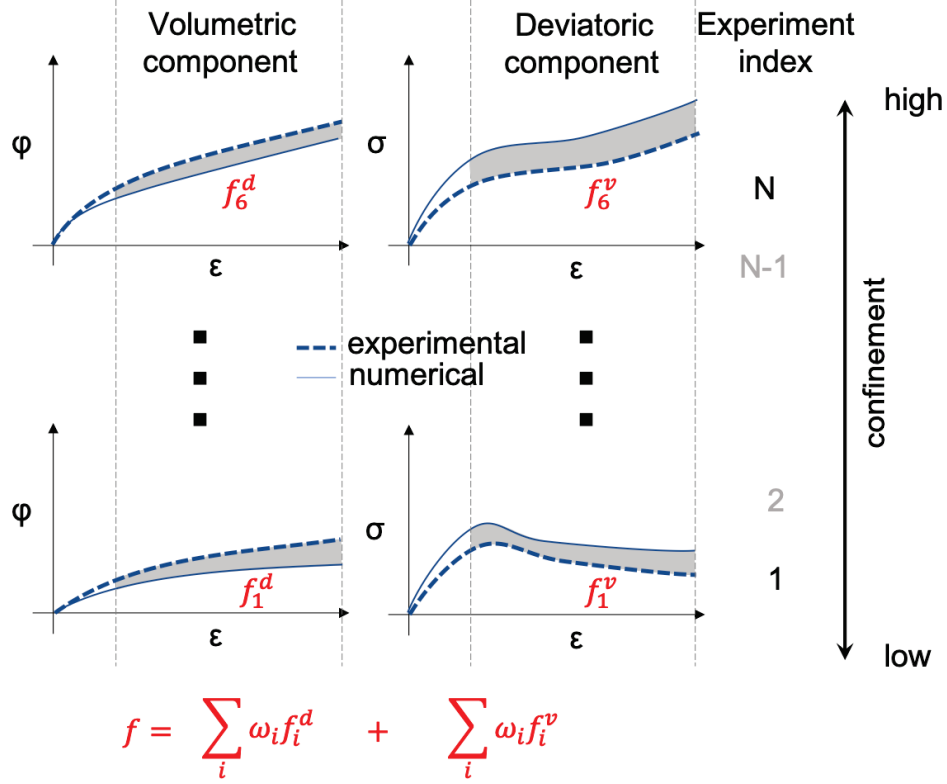


Figure 3.2: Schematic description of the objective function (f) computation, showing its volumetric and deviatoric components for a series of experiments at various confinements. See the full explanation in Sec. 3.3.

as the sums of all components for all confining pressures, $f^d = \sum_{i=1}^N \omega_i f_i^d$ and $f^v = \sum_{i=1}^N \omega_i f_i^v$, using a family of weights $\{\omega_i\}_{1 \leq i \leq N}$ which typically reduces the emphasis on the low values of confinement where the physical model is less adapted. In the two case studies presented in this work, the weights values of the objective function were selected as $\{0.2, 0.5, 1, 1, 1, 1\}$ to reduce the impact of the experiments at the lower confinements.

In order to respect some balance between the volumetric and deviatoric components, the values of stress and porosity used in the definition of the errors are normalised so their maximum ranges are identical. The total objective function is taken as the sum of the deviatoric and volumetric components, $f = f_d + f_v$.

3.3.1 Pseudocode for the objective function

```
def plastic_norm(result, reference):
    result = extract_plastic_portion(result)
    reference = extract_plastic_portion(reference)
    return L2norm(result.volumetric_stress, reference.volumetric_stress) +
           L2norm(result.deviatoric_stress, reference.deviatoric_stress)

def calculate_objective_function(input_params, reference_experiments):
    //this function performs a series of simulations at different confining
    //pressures, using input_params, and compares them to a corresponding
    //set of reference triaxial experiments

    //run each of the six simulations to obtain results as time series
    sim_result_CD1 = run_simulation(input_params, confining_pressure_CD1)
    sim_result_CD2 = run_simulation(input_params, confining_pressure_CD2)
    sim_result_CD3 = run_simulation(input_params, confining_pressure_CD3)
    sim_result_CD4 = run_simulation(input_params, confining_pressure_CD4)
    sim_result_CD5 = run_simulation(input_params, confining_pressure_CD5)
    sim_result_CD6 = run_simulation(input_params, confining_pressure_CD6)

    //calculate a plastic norm for each set of results by
    //comparing it to the reference physical experiments
    objective_CD1 = plastic_norm(sim_result_CD1, reference_experiment.CD1)
    objective_CD2 = plastic_norm(sim_result_CD2, reference_experiment.CD2)
    objective_CD3 = plastic_norm(sim_result_CD3, reference_experiment.CD3)
    objective_CD4 = plastic_norm(sim_result_CD4, reference_experiment.CD4)
    objective_CD5 = plastic_norm(sim_result_CD5, reference_experiment.CD5)
    objective_CD6 = plastic_norm(sim_result_CD6, reference_experiment.CD6)

    //the objective function is a weighed average of the six experiments
    return (0.2 * objective_CD1 + 0.5 * objective_CD2 +
            objective_CD3 +         objective_CD4 +
            objective_CD5 +         objective_CD6)
```

Chapter 4

Pathfinder 2.0

4.1 Heuristics and automation: a hybrid strategy

Enumerating all the sources of uncertainty, it becomes obvious that a brute force approach of attempting all possible parameter combinations would be prohibitively expensive from a computational point of view. At the same time, it would not necessarily provide theoretical modellers with too much insight into the complex couplings involved and the respective importance of all parameters, which is an important part of the longer-term strategy behind this work, as stated in Sec. 2.1.

To calibrate a complex THM model from experimental data, significant work needs to go into dimensionality reduction. A divide-and-conquer approach is needed for breaking the problem into more tractable sub-problems. At the same time, there are structures, regularities and rules-of-thumb in the problem that can be learned over time, by observing simulation outputs, that can help narrow down the search space. Involving humans in the optimization process has several advantages: humans have existing subject knowledge that is difficult to completely encode into programs. Humans are better at spotting trends and novelties, and making intuitive judgement on which parts of the search space to explore first. Finally, considering that the goal is to understand the underlying scientific principles, a human-explainable model can be much more valuable than a black-box neural network that cannot necessarily be generalized.

On the other hand, it is widely recognised that keeping humans in the loop creates many drawbacks, which explains the rapidly expanding global trend towards automation. The process of running these simulations is complex, with many small yet vital details. Humans can make mistakes, forget things, and lose track of data. Humans have difficulties doing things in a reproducible manner, and are much slower than computers. In a multi-step process like this, mistakes in any step can compound,

and result in nonsensical results - "Garbage In, Garbage Out" (Babbage & Baudouin, 2009).

To mitigate these challenges, It is necessary to automate repetitive tasks as much as possible, thus reducing human interaction to a minimum. To this end I developed Pathfinder 2.0, which is a suite of tools for developing, running, interpreting and optimizing simulations in REDBACK. It is a much-improved version of the code outlined in (Lin et al., 2017), and helps guide every step of this workflow. The goal is to reduce human intervention to deciding on a few critical numbers based on high-level interpretation of the results, with all the implementation details and settled science abstracted away.

4.2 Scientific workflows

Scientific workflow systems are an application of workflow management softwares and systems to solving scientific problems, reproducibly executing a series of computational or data management steps, or workflow. The design of scientific workflow systems is an established field, with many software packages available, such as Pegasus (Deelman et al., 2015), Kepler (Ludäscher et al., 2006), Taverna (Wolstencroft et al., 2013), Nimrod/K (Abramson et al., 2008), to name a few. A recent overview of workflow softwares, their development and the challenges they face can be found in (Liew et al., 2016).

In the case of Pathfinder, I did not rely on existing workflow systems but developed instead a customised one. The existing scientific workflow frameworks try to cover a broad range of use-cases, and this makes them heavyweight and complex, with a correspondingly steep learning curve and room for unexpected behaviour. They can result in savings in time and money mostly when they are used to implement long and complex workflows, where the initial learning curve is mortgaged over a long development process. In contrast, the workflow described in this work is quite straightforward from a programming perspective, and by coding it myself I avoid the incidental complexity of having to interact with a large external framework. Further, the development of this workflow demands an agile process, as it must iterate very quickly whenever the model changes. Coding from scratch gives fine-grained control over every detail, facilitating rapid prototyping.

4.3 Meeting requirements

Pathfinder sets out to solve several problems, specific to the needs of REDBACK model development:

- **Multi-platform.** The software needs to work both locally and remotely. It needs to work on HPC platforms, each of which has its own requirements/details in terms of job submission process, node and queue design, and software environment. The development of REDBACK happens on several platforms, both local on Linux and macOS, and remotely on HPC platforms such as Leonardi@UNSW, Raijin@NCI and Magnus@Pawsey. Leonardi is a faculty cluster based in UNSW, spanning a few dozen nodes. Raijin is a 84,656-core Fujitsu/Lenovo cluster based in the ACT. Magnus is a Cray XC40 system based in Perth.
- **Flexible.** The underlying model changes frequently. The simulations in this work rely on MOOSE and REDBACK, both open-source projects constantly being updated. The software needs to evolve along with the model and parent softwares. It needs to be flexible enough to survive constant changes.
- **Useful.** The software needs to automate away menial tasks (such as precalculation, post-processing, etc.) as much as possible. At minimum, it needs to meet or beat the previous, manual process at every step.
- **Not a black box.** The users must be kept in-the-loop and well-informed. For example, users need to be able to break open the data pipeline at any point and examine the contents, to make sure everything is working the right way. There also need to be clear separation between the menial tasks that can be performed by a computer, and significant decisions that require domain knowledge.

All those developments were met:

- **Multi-platform.** As part of the workflow development, I deployed and tested MOOSE/REDBACK on several platforms, both PCs (Linux, macOS) and clusters (Leonardi, Raijin, Magnus). Pathfinder is implemented as a collection of Python 2.x scripts, as MOOSE and REDBACK already requires a Python 2.x installation. Pathfinder is designed to function without additional software installs, and has few additional requirements on top of those of MOOSE/REDBACK. Any potential slowdowns caused by using an interpreted language such as Python is considered insignificant compared to the very demanding REDBACK simulations. The simulation management module abstracts away the architecture-specific implementation details, so that the users can focus on the science.
- **Flexible.** Pathfinder has witnessed and adapted to many model changes, improving alongside the theoretical understanding. It is impossible to set out to

make something that never changes when the parent does (since you don't know what will change), but Pathfinder is flexible enough to change along with the theory.

- **Useful.** The usefulness of Pathfinder is best demonstrated by the results presented in this work. They would not have been possible if I stayed on the old, manual process. Pathfinder greatly increased the speed of iterations between theory and testing, and at the same time it organized and kept track of the many vital details of the model, leaving less room for human error and forgetfulness. The use of version control meant that all simulations are now reproducible, despite frequent changes.
- **Not a black box.** Pathfinder is designed from the ground up with a knowledgeable user in mind, and is not a 'press button and forget' solution. In Pathfinder the human is kept in the loop as much as possible, and processing steps that can potentially change the interpretation of data are kept transparent to the user. As a design decision, Pathfinder is constructed using very simple techniques and algorithms, and there are few moving pieces. This means it is easy for end-users to identify and understand any part of the code, see the exact functioning of the program, and extend/modify as necessary.

4.4 Components of Pathfinder

Pathfinder is implemented as a collection of Python 2.x scripts, in order to utilize the same version of Python as MOOSE and REDBACK. Pathfinder has several major components to interact with the various aspects of the workflow, including the pre-processing, simulation management, parameter optimisation and post-processing.

4.4.1 Pre-processing

Pathfinder aids in initializing the physical and experimental parameters. Instead of having an input file with potentially hundreds of fields as in REDBACK, Pathfinder abstracts away most of the detail. REDBACK is a general-purpose simulator, that can simulate a wide range of multiphysics scenarios, across many scales, materials, and experiment setups. This flexibility comes hand-in-hand with additional complexity. An input file describing a specific experiment schedule including material properties, geometry, boundary conditions and numerics-related properties can easily go to hundreds of lines, all of which impacts the end-result. By narrowing the focus to a specific type of experiment (in this case, consolidated-drained triaxial tests, though other experiments are also possible), Pathfinder can cut down on this complexity. For example,

Pathfinder separates the parameters that rarely or never change (e.g. physical constants, parameters describing the experiment setup) from the handful of constitutive parameters that are complete unknowns (to be scrutinized manually or via parameter inversion). Co-dependent parameters (see Chapter 2) are pre-calculated and normalization (see Eq. 2.2 and Eq. 2.4) is done automatically, as the equations for them are largely not subject to change.

In practice, the boundary between settled and unknown parameters is blurred, and reflect current understanding and assumptions. As this understanding changes, Pathfinder is updated to add or remove parameters from the list needing close scrutiny, or change the equations used. Unlike a paper record, Pathfinder is tied directly to numerical simulations that give feedback to end-users, so any errors, ambiguities and inconsistencies are much more easily discovered. In this way, Pathfinder becomes a programmatic description of the current state-of-art of the model, facilitating communication and knowledge transfer.

4.4.2 Simulation management

REDBACK simulations used in this work can each be scaled from one to hundreds of CPUs, and an optimization run can involve hundreds or thousands of these simulations. Access to HPC platforms is metered, so it is vital to orchestrate these simulations in an efficient way. Pathfinder handles running large numbers of simulations and orchestrating parameter inversion tasks on HPC platforms, abstracting away the local, architecture-dependent implementation details, including the handling of the queuing system, the number of CPUs and nodes of the host and other parallelization settings. It schedules REDBACK simulations automatically in a way that optimizes resource usage.

Reproducibility and change-tracking is vital, and this component also handles the management of simulation results. Source code is version-controlled using industry-standard Git (*git(1) Manual Page*, 2019). Simulation results are stored and indexed together with its input parameters, so that any set of simulations can be re-ran as needed.

4.4.3 Parameter optimization

Considering the "no-free-lunch theorem" (Wolpert & Macready, 1997), no inversion strategy performs better than all others in all cases. Instead, the choice of algorithm depends on the problem at hand. Several widely-used algorithms were considered for implementing the optimization routine, including Nelder-Mead (Nelder & Mead, 1965), Stochastic Gradient Descent (Robbins & Monro, 1951), Broyden-Fletcher-Goldfarb-Shanno

(BFGS) (Broyden, 1970), Genetic Algorithm (Holland, 1992), and Particle Swarm (PSO) (Kennedy & Eberhart, 1995), though gradient-based algorithms such as Stochastic Gradient Descent and BFGS were eliminated from consideration due to issues with noisy and unreliable gradient information, causing the optimizer to fall into local minima.

Following (Nguyen-Tuan et al., 2016), where a similar inverse THM problem is investigated, Pathfinder’s inversion strategy is using PSO, which has been proven to be a suitable choice where the complexity of the forward problem supports the assumption of a non-convex optimisation problem. From an implementation perspective, PSO supports running a large number of simulations in parallel, meaning it scales easily in highly parallel high-performance computing (HPC) environments. It is also a simple enough algorithm to be implemented without relying on external programs other than a lightweight library, Pyswarm (tisimst, 2019), which simplifies the design and implementation. The exact procedure and objective function used is covered in Chapter 3. An illustration of the interactions between this module and the simulation management module is shown in Fig. 4.1.

PSO has tunable parameters to control various behaviours of the algorithm. For example, hyperparameters p and g control the ‘force’ attracting particles to their own best result, and the global best result, respectively. The difference between good and bad values of such parameters can trigger large differences in convergence speed. To tune these parameters, synthetic data sets were first constructed by varying two parameters (α_1, α_2) in REDBACK simulations in a grid pattern that includes a known cost minima. The grid is filled by calculating the cost functions for each simulation, then interpolating the values between them via a radial basis function (Broomhead & Lowe, 1988), implemented using (*scipy.interpolate.Rbf*, 2019). Next, repeated PSO runs with random starting points were performed on these synthetic data-sets in a grid-search to find the set of hyperparameters that minimizes average number of iterations to convergence. The result is a map of convergence iterations as function of α_1 and α_2 (see Fig. 4.2). Since the physical model itself is subject to the inversion process, it is very challenging to get the absolute best set of hyperparameters for any given optimization run without spending more compute power than the value of information (realistic synthetic data generation requires large number of REDBACK simulations, and would need to be re-done for a change in physical model), but going through this hyperparameter tuning even a small number of times prevents common pathological cases that would cause the algorithm to get stuck or take more time than necessary, such as the large region on the left side in Fig. 4.2.

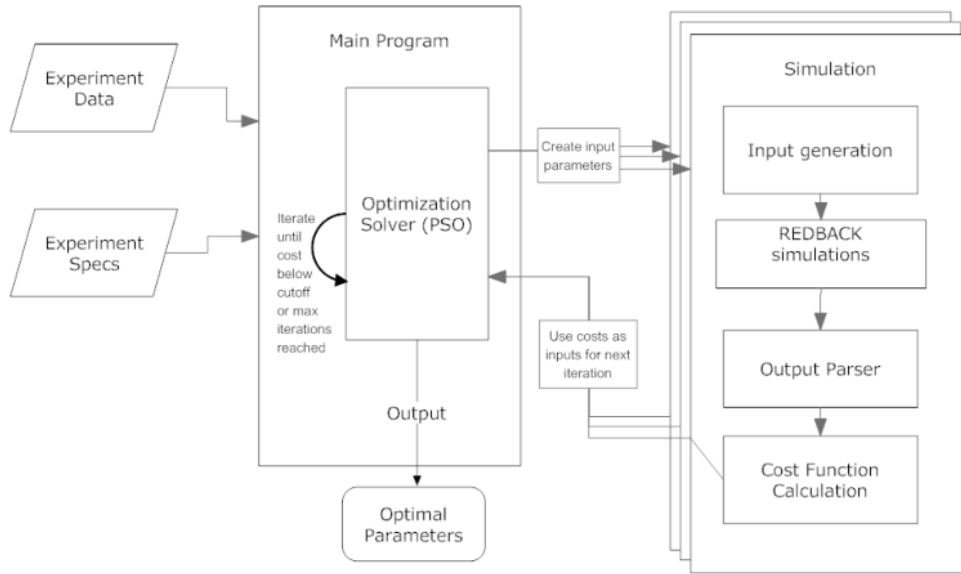


Figure 4.1: Parameter inversion in Pathfinder, reproduced from (Lin et al., 2017).

Iterations to convergence

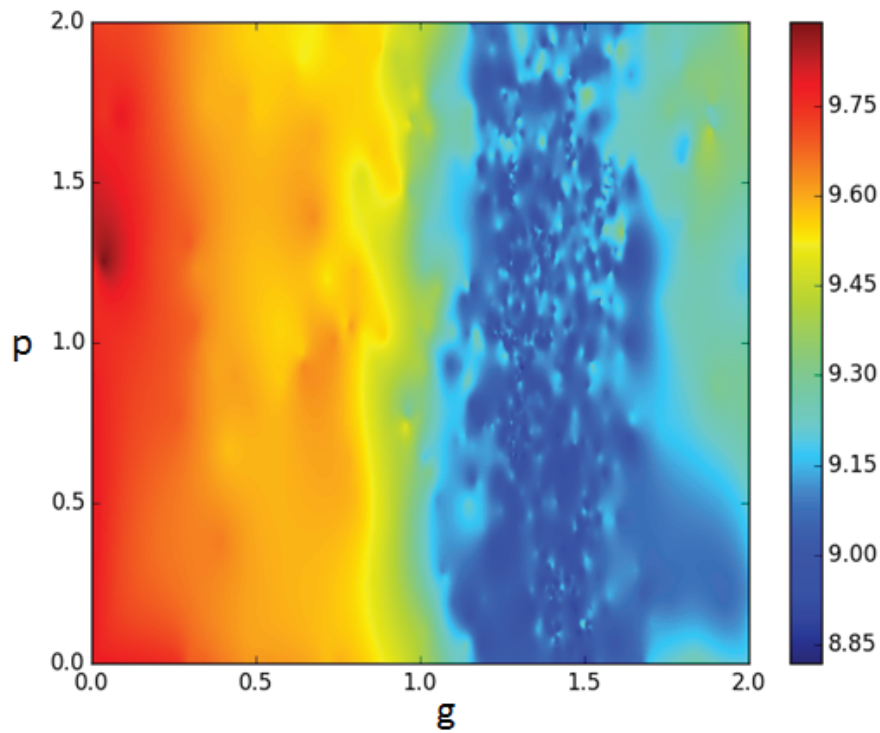


Figure 4.2: Grid search on PSO hyperparameters

4.4.4 Post-processing

The final component runs locally on the user's personal computer, to generate various plots and graphics from the output files generated by REDBACK. The manual workflow Pathfinder replaced involved the user downloading the results, clean and aggregate them, then generate the plots in Excel. This module simply automates this process. Many of the figures in this work are generated using Pathfinder. The graphics are plotted using Python's Matplotlib library, with post-processing using Scipy and Scikit-learn.

Chapter 5

Case study: Noto diatomaceous mudstone

In this case study, I apply the workflow developed in Chapter 3 to fit experimental results from experiment data on mudstone published by Oka et al. (2011).

5.1 Rock description

The material used in this study is Noto diatomaceous mudstone, whose properties are described in details in (Maekawa & Miyakita, 1983). It is composed of 1% sand, 66% silt and 33% clay. In particular, it is characterised by its high porosity (73%) and permeability ($1.55 \times 10^{-9} m^2$). Oka's team submitted this rock to conventional consolidated-drained (CD) shear tests to observe the rock behaviour under various confinements.

5.2 Triaxial experiment description

A series of tests was performed, at six effective confinement pressures of 0.25 MPa (CD1), 0.5 MPa (CD2), 0.75 MPa (CD3), 1 MPa (CD4), 1.5 MPa (CD5) and 2 MPa (CD6) respectively. The pore fluid was water. An ambient temperature of 20 degrees Celsius is assumed. The samples were 4cm x 4cm x 8cm rectangular prisms. A description of the triaxial apparatus for testing prismatic samples is provided in (Oka et al., 2011).

Each experiment was split into two stages: an initialisation step followed by the main compression experiment. Stage one took 6 hours, under isotropic conditions, with constantly increasing confining pressure until target confinement was reached. In stage two, constant confinement was applied under drained conditions; Compression from

Case No.		CD1	CD2	CD3	CD4	CD5	CD6
Effective confining pressure	σ'_{m0} (MPa)	0.25	0.50	0.75	1.00	1.50	2.00
Initial elastic shear modulus	G_0 (MPa)	92.000	92.000	92.000	92.000	92.000	92.000
Compression index	λ	1.292	1.292	1.292	1.292	1.292	1.292
Swelling index	κ	0.0487	0.0487	0.0487	0.0487	0.0487	0.0487
Initial void ratio	e_0	2.72	2.72	2.72	2.72	2.72	2.72
Compression yield stress	σ'_{mai} (MPa)	2.55	2.55	2.55	2.55	2.55	2.55
Stress ratio at maximum compression	M_m^*	1.551	1.551	1.551	1.551	1.551	1.551
Viscoplastic parameter	m'	28.76	28.76	28.76	28.76	28.76	28.76
Viscoplastic parameter	C_1 (s ⁻¹)	1.0×10^{-6}	1.0×10^{-6}	1.0×10^{-6}	1.0×10^{-6}	1.0×10^{-6}	1.0×10^{-6}
Viscoplastic parameter	C_2 (s ⁻¹)	7.0×10^{-6}	1.5×10^{-6}	1.2×10^{-6}	1.2×10^{-6}	1.2×10^{-6}	1.2×10^{-6}
Structural parameter	σ'_{maf} (MPa)	1.00	1.60	1.80	1.90	2.10	2.20
Structural parameter	β	7.5	7.0	7.0	6.0	3.0	2.0
Coefficient of permeability	k (m/s)	1.55×10^{-9}	1.55×10^{-9}	1.55×10^{-9}	1.55×10^{-9}	1.55×10^{-9}	1.55×10^{-9}
Poisson's ratio at initial state*	$v _{\text{initial}}$	-0.424	-0.168	-0.023	0.070	0.183	0.249
Poisson's ratio at an axial strain of 20%*	$v _{20\%}$	-0.223**	-0.058	0.038	0.106	0.190	0.242

* $v = (3K - 2G)/(2(3K + G))$, $K = (1 + e)\sigma'_m/\kappa$.

**Poisson's ratio at the peak stress for the case CD1.

Figure 5.1: Physical parameters for triaxial experiments; excerpted from (Oka et al., 2011)

the top proceeded for approximately 33 hours and 20 minutes, at constant displacement of 0.01%/min and the maximum axial strain reached approximately 20%. Physical parameters reported by the authors for those experiments are listed in 5.1.

Figure 5.2 shows the evolution of deviatoric stress with axial strain for all six experiments. The results demonstrate nicely the existence of a characteristic point for each experiment (before 2% axial strain) where the initial linear elastic behaviour switches to what is usually described as a plastic regime. The same transition can be observed when plotting the volumetric strain against the mean effective stress (Figure 5.2, lower). It is notable that all six experiments are in the compactant regime where total volume decreases over the course of experiments. In the absence of unloading data, this transition from linearity is usually interpreted as a yield point marking the start of plasticity for the overall sample and can be plotted over the loading path

and linked to obtain a yield envelope as shown in Figure 5.3. The shape of this yield envelope is characteristic of a compression cap, with the yield point diminishing with increased confinement and a final value of mean effective stress obtained through an isotropic compression experiment.

Another important point to note from the experimental results is that the evolution of deviatoric stress in the plastic regime is quite sensitive to the value of confinement, ranging from a strong weakening behaviour at low confinement (CD1) to strong hardening for higher confinements.

5.3 Simulation and parameter inversion

The strain-stress results from those experiments were previously used to calibrate an earlier version of the model described in (Poulet & Veveakis, 2016). In this work, the volumetric responses are also considered as extra simultaneous constraints.

The experimental results from (Oka et al., 2011) indicate the suitability of the extended modified Cam-Clay yield envelope (see Sec. ??) for the whole sample. A first set of numerical values is derived to match the experimental yield points reported by Oka et al. (2011): $M = 1.2$, $p_c = 2.26MPa$, $p_t = -0.68MPa$, $\gamma_1 = 0$ and $\gamma_2 = 1e6$. Note that the large value of γ_2 basically produced a traditional Modified Cam-Clay envelope. Based on the discussion from Sec. ?? I conjecture a similar but smaller shape for the yield envelope needed for the numerical simulations, keeping only a single free scaling parameter since keeping the same pre-consolidation pressure ultimately proved adequate. This is shown in Fig. 5.4. The mesh used in this study is shown in Fig. 5.5.

Following the inversion process described in Chapter 3 leads to the final parameters listed in table 5.1, providing acceptable fits for both sets of curves shown in Fig. 5.6 and Fig. 5.7.

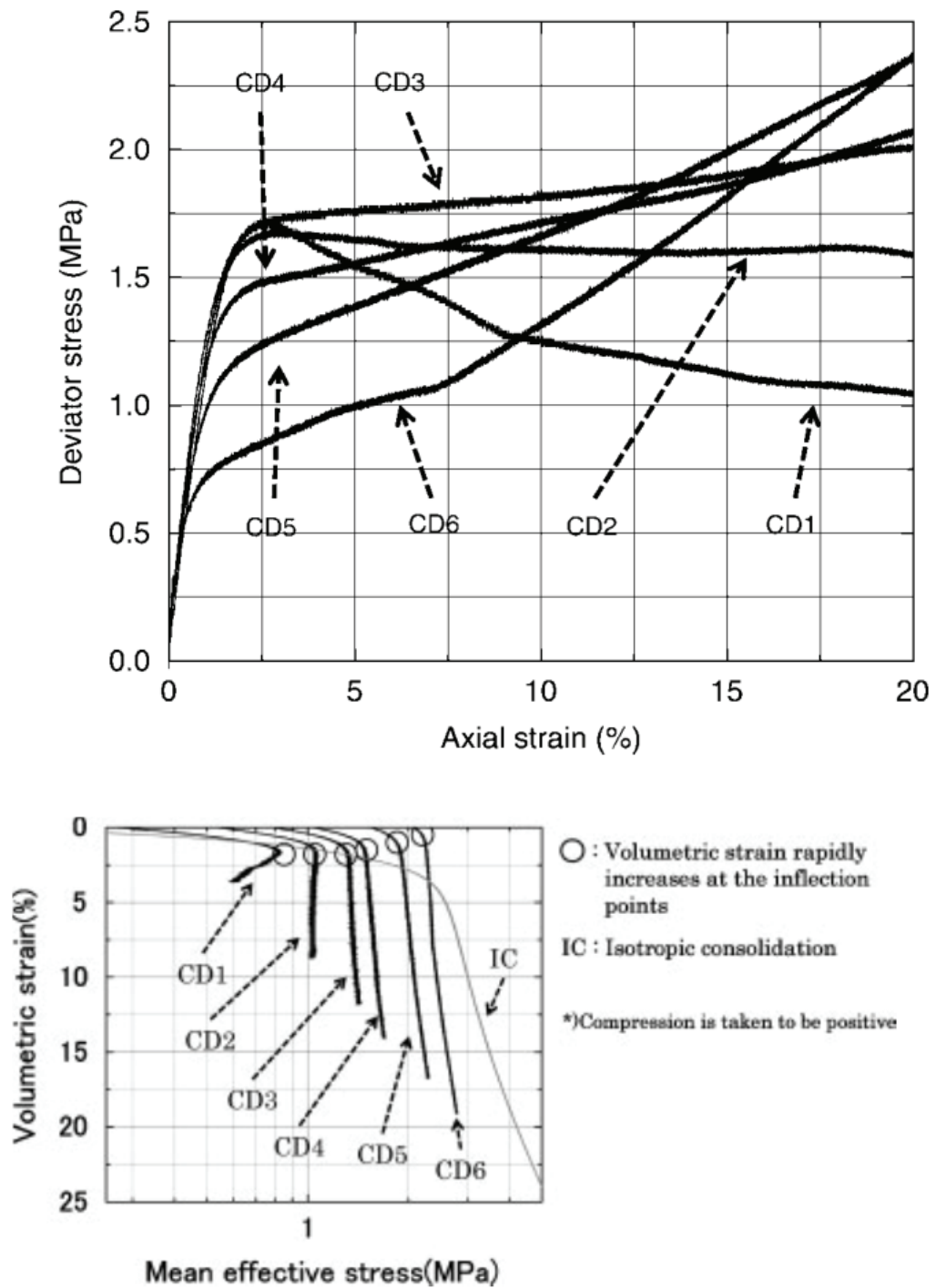


Figure 5.2: Experiment responses in consolidated-drained CD triaxial tests, excerpted from (Oka et. al, 2011)

Parameter name	Symbol	Value	Unit of Measure
Flow law overstress exponent	m	2	-
Initial permeability	κ	1.55×10^{-9}	m^2
Initial porosity	ϕ	0.74	-
Arrhenius coefficient	Ar	8	-
Young's modulus	E	135.6	MPa
Poisson ratio	ν	0.2	-
Fluid thermal diffusivity	$c_{th,f}$	1.43×10^{-7}	$m^2.s^{-1}$
Fluid thermal expansion coefficient	λ_f	6.9×10^{-5}	K^{-1}
Fluid viscosity	μ, f	8.9×10^{-4}	$Pa.s$
Fluid compressibility	β_f	4.5×10^{-10}	Pa^{-1}
Solid thermal diffusivity	$c_{th,s}$	1.64×10^{-6}	$m^2.s^{-1}$
Solid thermal expansion coefficient	λ_s	5×10^{-6}	K^{-1}
Solid compressibility	β_m	3.46×10^{-7}	Pa^{-1}
Mixture thermal diffusivity	$c_{th,m}$	5.45×10^{-7}	$m^2.s^{-1}$
Mixture thermal expansion coefficient	λ_s	5.18×10^{-5}	K^{-1}
Mixture compressibility	β_m	9.34×10^{-8}	Pa^{-1}
Mixture thermal pressurisation coefficient	Λ_m	555	$Pa.K$
Lewis number	Le	50	-
Gruntfest number	Gr	3.3×10^{-3}	-
Yield envelope, tension cut-off	p_t	-0.68	MPa
Yield envelope, pre-consolidation pressure	p_c	2.26	MPa
Yield envelope, slope of critical state line	M	0.24	-
Yield envelope, γ_1 parameter	γ_1	10	-
Yield envelope, γ_2 parameter	γ_2	-31.4	-

Table 5.1: Parameter values obtained for the fits of mudstone experiments shown in Fig. 5.6 and Fig. 5.7.

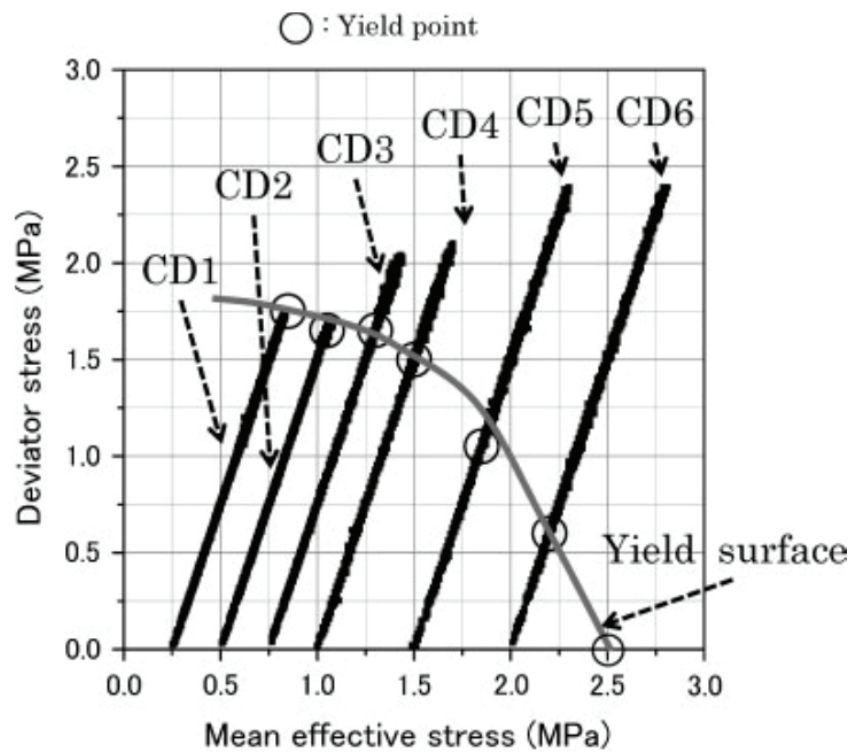


Figure 5.3: Effective stress paths and yield surface in triaxial tests, (Oka et. al, 2011)

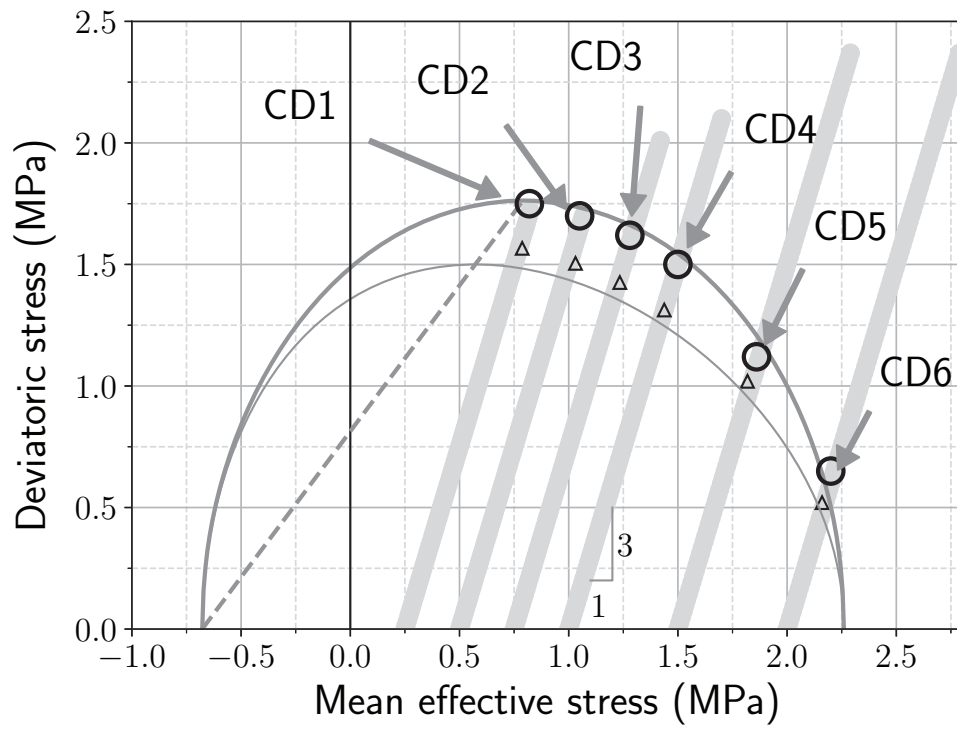


Figure 5.4: Experimentally determined yield points (black circles) for mudstone by Oka et al. (2011) and corresponding yield envelope (thin line), as well as result yield envelope (thick line) obtained from the inversion process, scaling the experimental yield envelope along the Critical State Line (dashed line). The thick lines in light grey show the stress paths for all confined drained experiments CD1-6. The triangles mark yield points obtained from the experimental data at 0.2% plastic strain.

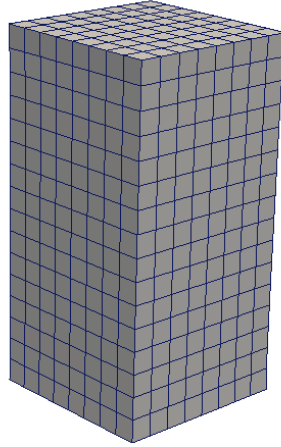


Figure 5.5: 3D mesh used in FEM simulations of Noto mudstone

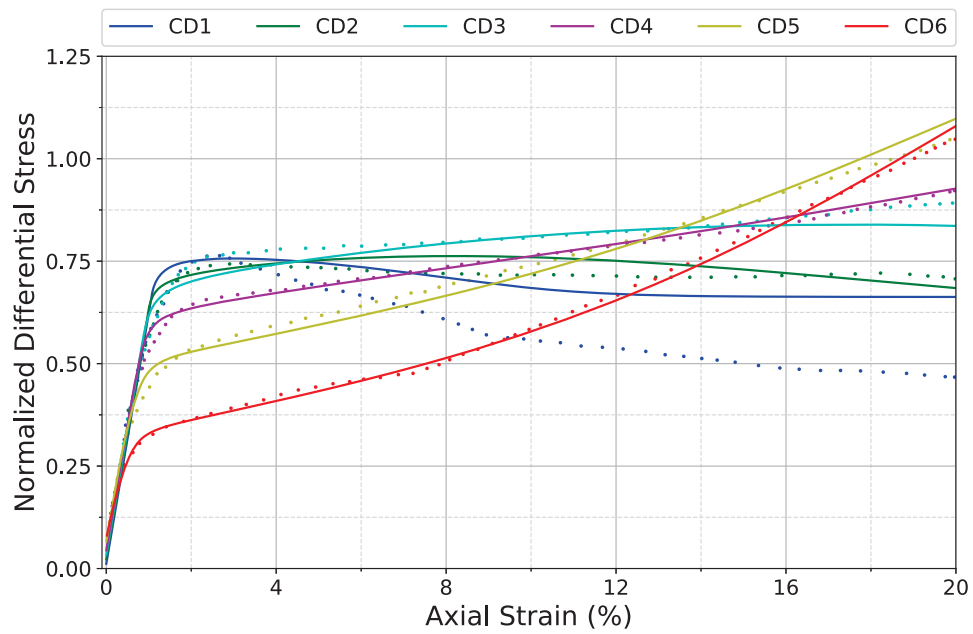


Figure 5.6: Deviatoric stress as function of axial strain at various confinements; comparison of numerical (solid lines) and experimental results (dashed lines).

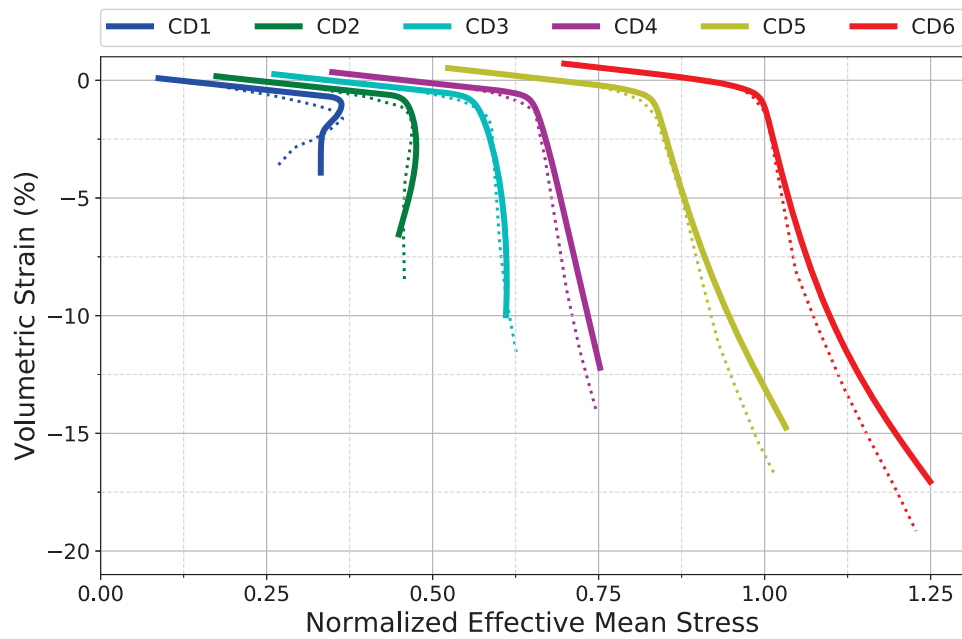


Figure 5.7: Volumetric strain curves in function of mean effective stress at various confinements for mudstone; comparison of numerical (solid lines) and experimental results (dashed lines).

Chapter 6

Case study: Adamswiller sandstone

In this case study I apply the Pathfinder workflow to fit experimental results from experiment data on Adamswiller sandstone (T.-F. Wong et al., 1997), a much harder material, to show that the workflow can operate in a wide range of conditions.

6.1 Rock description

Adamswiller sandstone is composed of 71% quartz, 11% clay, 9% feldspar, and 5% oxides and mica. Cylindrical samples are cut from cores parallel to bedding.

Adamswiller sandstone has been studied extensively, and detailed physical properties can be found in a series of papers by T.-F. Wong et. al, including (David et al., 1994), (T.-F. Wong et al., 1997), (Zhu & Wong, 1997),(T. Wong & Baud, 1999),(Tembe et al., 2007) and (Zhu et al., 2008).

This rock was subjected to conventional consolidated-drained (CD) shear tests to observe its behaviour under various confinements.

6.2 Triaxial experiment description

Six experiments were performed at different effective confinement pressures of 5 MPa, 20 MPa, 40 MPa, 60 MPa, 100 MPa, and 150 MPa; referred to as CD1 to CD6 respectively. The samples were cylinders with diameter of 18.4 mm and length of 38.1 mm. All samples were fully saturated with water. T.-F. Wong et al. (1997) report all experiments were performed at 'room temperature', so an ambient temperature of 20 degrees Celsius is assumed. The authors also report Young's moduli of 5.69 GPa,

8.03 GPa, 7.78 GPa, 10.36 GPa, 10.38 GPa, 10.54 GPa respectively for the six samples; For the rest of this work I assume a value of 10 GPa for simplicity.

All experiments are performed in two stages: stage one is under isotropic conditions, with constantly increasing confining pressure until target confinement is reached. In stage two, constant confinement was applied under drained conditions. Similarly, for the numerical simulations, each experiment was split into two stages: an initialisation step followed by the main compression experiment. For the second stage, a strain rate of $4 \times 10^{-5} s^{-1}$ was reported; compression is carried out to more than 15%, or until the sample fails. This translates to a duration of 62.5 minutes for 15% strain. No duration was specified for the first stage; For the purpose of this study I assume a duration of 9 minutes.

The results of the six confined drained experiments are presented in (T.-F. Wong et al., 1997) and (T. Wong & Baud, 1999), some of them are reproduced here for comparison purposes. Figure 6.1 shows the evolution of deviatoric stress and porosity with axial strain for all six experiments. The authors report that CD1-3 failed by shear localization, while CD4-6 failed by compactive cataclastic flow. The six experiments span the range of behaviours from brittle to ductile, exhibiting the characteristic signatures of both regimes. In CD1 the steep drop in deviatoric stress between 2 MPa and 3 MPa is typical of a brittle behaviour. In the brittle failure regime (CD1-3), the transition from elastic to plastic regime is marked by a stress overshoot. For more ductile regime (CD5,6) the response is more regular, and shows some hardening.

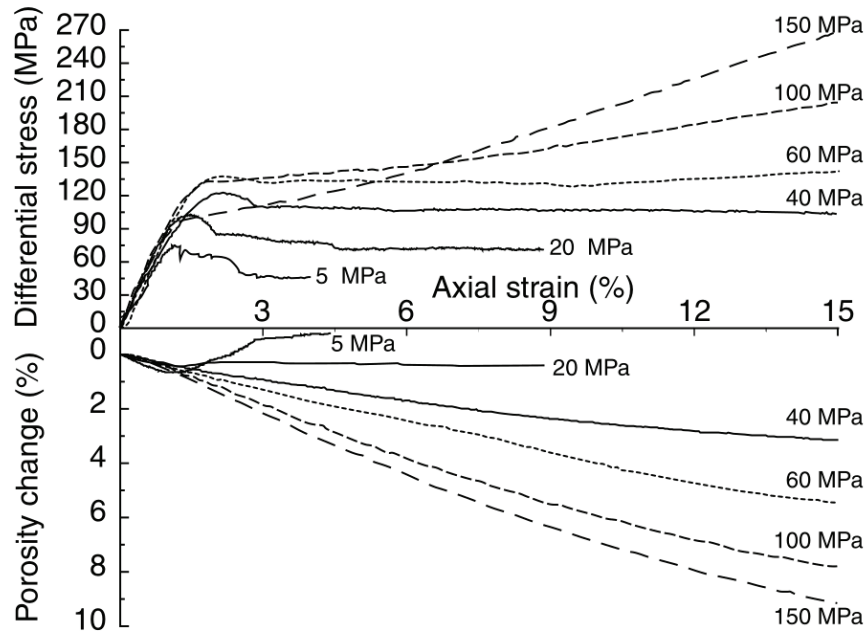


Figure 6.1: Stress-strain behaviour in consolidated-drained CD triaxial tests, (T. Wong & Baud, 1999). The solid curves are for samples which failed by shear localization, and the dashed curves are for samples which failed by cataclastic flow, with delocalized compaction and strain hardening.

From the results of triaxial and isotropic experiments, it is possible in theory to derive a yield point at each confining pressure, and a yield surface can be derived by interpolating between these yield points. The determination method of the yield point, however, is not standardised, and T.-F. Wong et al. (1997) select their yield points in two different ways. Yield points are chosen for all six experiments by picking the points on Fig. 6.2 where the experiments deviate from the isotropic response. For the low confinement regime (CD1,2,3), T.-F. Wong et al. (1997) additionally identify the peak deviatoric stresses for the low-confinement experiments which results in higher yield stresses. To close the yield envelope, the preconsolidation pressure P_c is selected as the turning point on the isotropic compression curve. This is marked as P^* on the second graph in Fig. 6.2. Fig. 6.3 shows the resulting yield points along with loading paths.

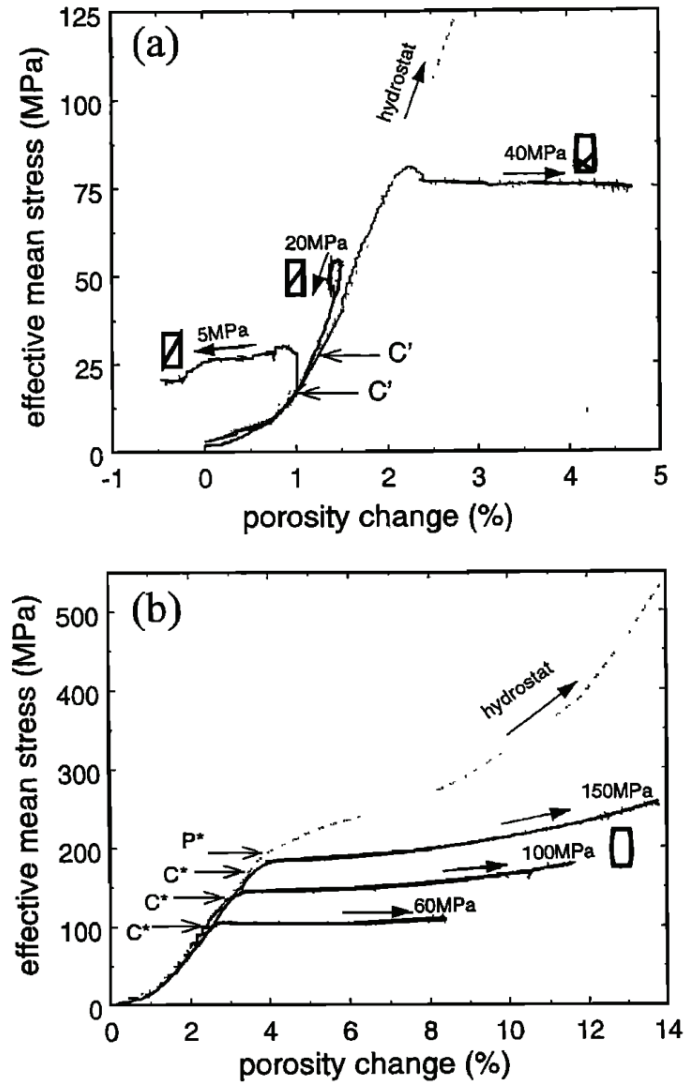


Figure 6.2: effective mean stress vs porosity change, reproduced from (Wong et.al, 1997)

6.3 Simulation and parameter inversion

The finite element simulation uses the mesh shown in Fig. 6.4. The inversion process followed the same steps described previously and led to the identification of the yield enveloped presented in Fig. 6.5, using this time the pre-consolidation value as a second free parameter. The numerical simulations show a good fit with experimental results, both for the deviatoric and volumetric responses, as shown in Fig. 6.6 and Fig. 6.7 respectively, for the corresponding parameter values listed in Table 6.1.

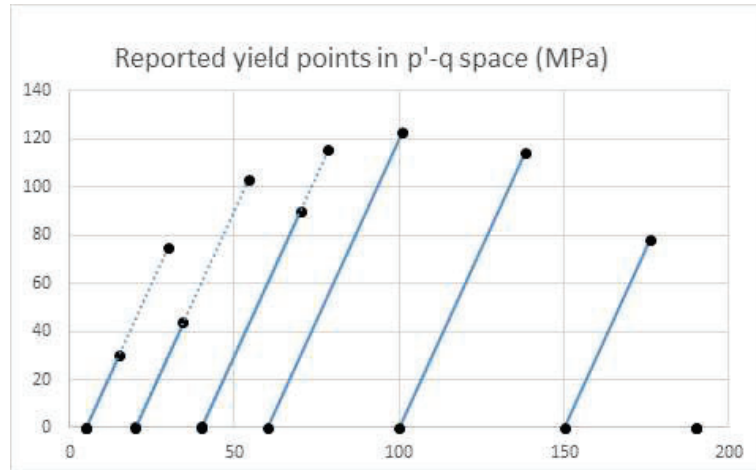


Figure 6.3: Reported yield points in $p' - q$ space

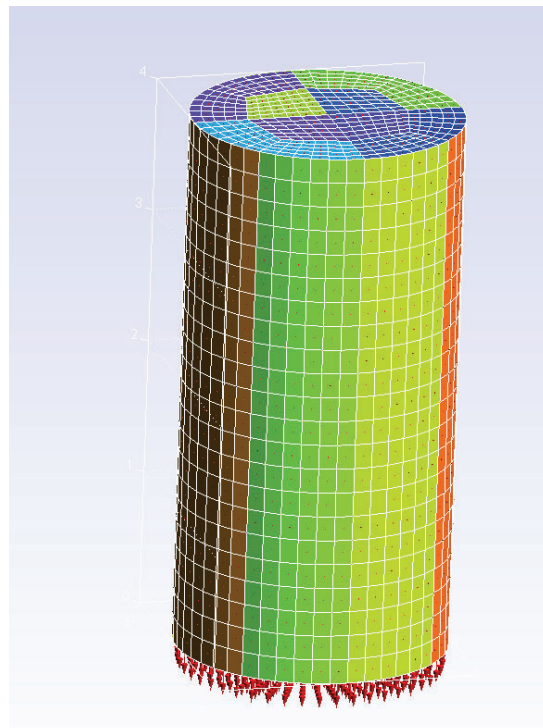


Figure 6.4: Finite Element mesh used for sandstone simulations

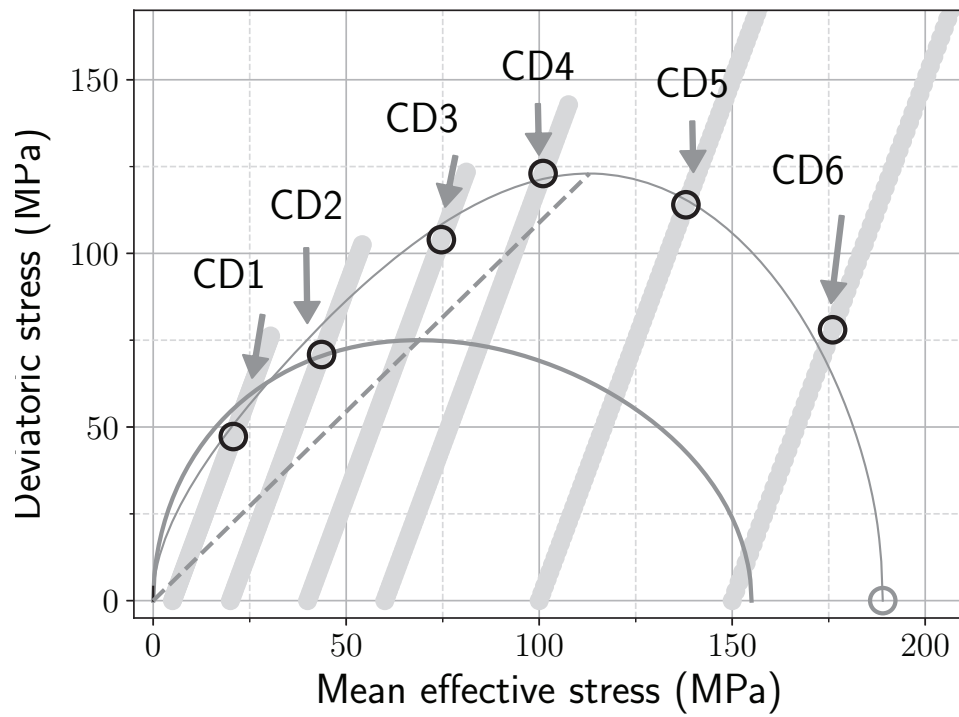


Figure 6.5: Experimentally determined yield points (black circles) for sandstone by (T.-F. Wong et al., 1997) and corresponding yield envelope (thick line), as well as result yield envelope (thin line) obtained from the inversion process, scaling the experimental yield envelope along the Critical State Line (dashed line) with a shift in pre-consolidation pressure. The thick lines in light grey show the stress paths for all confined drained experiments CD1-6.

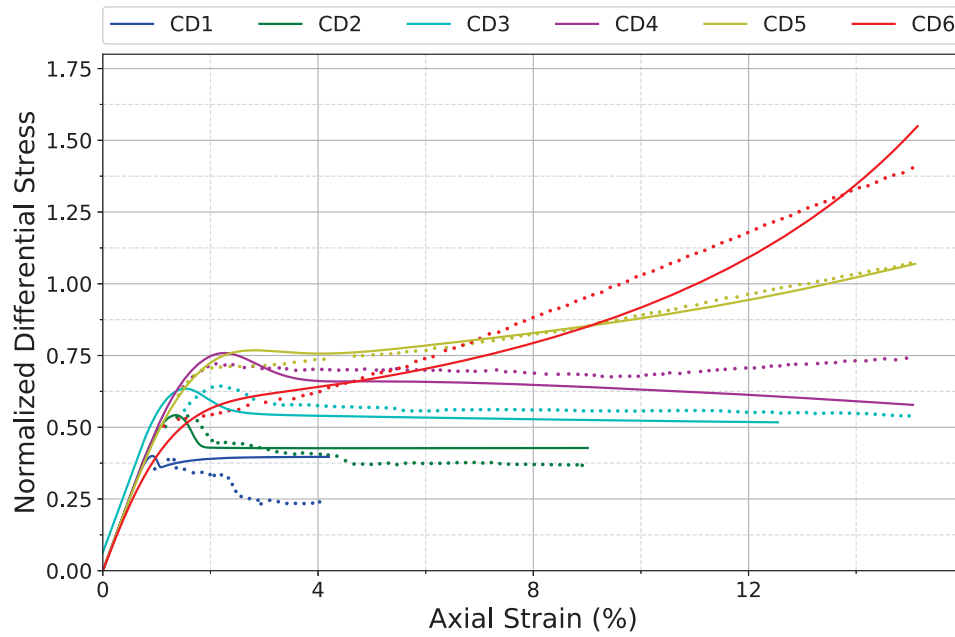


Figure 6.6: Stress strain curves at various confinements for sandstone; comparison of numerical (solid lines) and experimental results (dashed lines).

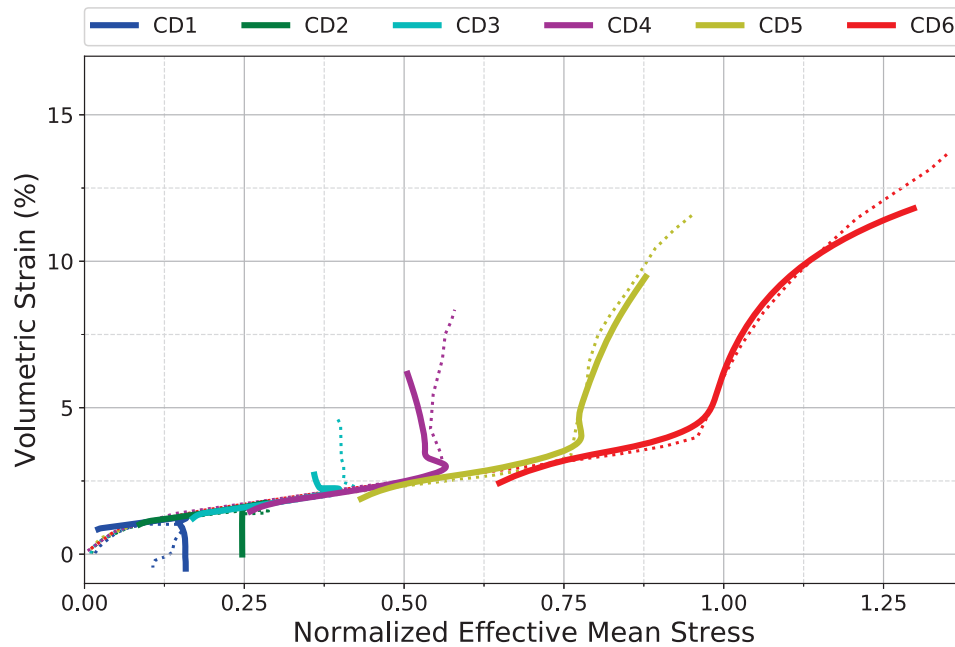


Figure 6.7: Volumetric strain curves at various confinements for sandstone; comparison of numerical (solid lines) and experimental results (dashed lines).

Parameter name	Symbol	Value	Unit of Measure
Flow law overstress exponent	m	2	-
Initial permeability	κ	1.48×10^{-14}	m^2
Initial porosity	ϕ	0.226	-
Arrhenius coefficient	Ar	6	-
Young's modulus	E	9.45	GPa
Poisson ratio	ν	0.2	-
Fluid thermal diffusivity	$c_{th,f}$	1.43×10^{-7}	$m^2.s^{-1}$
Fluid thermal expansion coefficient	λ_f	6.9×10^{-5}	K^{-1}
Fluid viscosity	μ, f	8.9×10^{-4}	$Pa.s$
Fluid compressibility	β_f	4.5×10^{-10}	Pa^{-1}
Solid thermal diffusivity	$c_{th,s}$	1.64×10^{-6}	$m^2.s^{-1}$
Solid thermal expansion coefficient	λ_s	3×10^{-5}	K^{-1}
Solid compressibility	β_m	1.9×10^{-10}	Pa^{-1}
Mixture thermal diffusivity	$c_{th,m}$	1.3×10^{-6}	$m^2.s^{-1}$
Mixture thermal expansion coefficient	λ_s	3.9×10^{-5}	K^{-1}
Mixture compressibility	β_m	2.5×10^{-10}	Pa^{-1}
Mixture thermal pressurisation coefficient	Λ_m	1×10^{-6}	-
Lewis number	Le	0.65	-
Gruntfest number	Gr	0.3	-
Yield envelope, tension cut-off	p_t	-5	MPa
Yield envelope, pre-consolidation pressure	p_c	155	MPa
Yield envelope, slope of critical state line	M	0.52	-
Yield envelope, α parameter	α	6	-
Yield envelope, β parameter	β	-24.7	-

Table 6.1: Parameter values obtained for the fits of sandstone experiments shown in Fig. 6.6 and Fig. 6.7.

Chapter 7

Flow law sensitivity analysis and saddle point

While this thesis focuses on a data-driven approach with an inversion workflow for multiphysics modelling of triaxial experiments, the longer-term goal behind this work is ultimately to extend the current physical understanding of rock plasticity. A model describing mechanical hardening and softening as a function of temperature and pressures would alleviate a major limitation of current models limited to interpolation between experimental results, to provide a model that can extrapolate beyond laboratory conditions.

Developing such a new theoretical model goes well beyond the scope of this thesis, yet it is important to note that data-driven and physics-driven approaches go hand in hand. The understanding of a given model behaviour and its limitations is a key factor in the development of an improved one and this chapter demonstrates the power of the inversion workflow to infer new information.

In the last three chapters I showed a workflow for calibrating the REDBACK model against experiment data, then showed two case studies that match the model closely against experiment data from well-known studies. In the pursuit of the longer-term goal to conjecture some physical knowledge from the numerical approach and try and reduce the number of laboratory experiments required to capture a rock behaviour, I used the calibration studies of Chapters 5 and 6 to assess whether it is possible to invert for α_1 and α_2 without relying on the experimental curves.

To this end, I added functionalities in Pathfinder to do the following:

- perform a sensitivity analysis by running a large number of simulations near the optimized results in α_1 - α_2 space
- generate maps of the objective function in α_1 - α_2 space via interpolation

- generate plots of each of many post-processors available per simulation in REDBACK, in the same space as above.
- identify characteristic points on simulation results (i.e. noisy data) to help users identify features of the objective function.

This is a purely data-driven exercise, not bound by any theoretical model. The goal is to identify any strong correlation, which would then guide the theoreticians in model development.

7.1 Parameter space

The flow law used in this work remains under active research and will most certainly continue to evolve in the near future. For instance, REDBACK's current energy-based model is most suited for pore-collapse type mechanism found in compaction and does not capture so well the behaviour in the dilatant regime, which is dominated more by geometry effects. This means that the model is more applicable at high rather than low confinement. The sandstone results contain a strain-hardening effect that is not currently captured in the model. Of the results presented, the mudstone results in high confinement (CD4-6) are most likely to be close to what the current theoretical model can capture. Therefore, the parameters used to simulate CD4-6 of mudstone were selected for this study. Note that the only change between these three sets of tests is the confining pressure.

Keeping all other parameters constant, a sensitivity analysis was performed on α_1 and α_2 (from Eq. 2.8) by taking 25 equally spaced values of those parameters within given ranges (α_1 in $[-8.5, -2.5]$, α_2 in $[0, 60]$) and running every other cross-product simulations to cover that parameter space. The 313 simulation results produced were subsequently compared against the experimental data using the objective function described in Sec. 3.3 to produce sensitivity maps presented in the following section.

7.2 Map of objective functions against experimental data

The experiments involve axial strain from 0% to 20%. It is possible to calculate an objective function (see Sec. 3.3) at any point in plasticity (after roughly 0.5% strain) by comparing against the experiment data from the onset of plasticity up to that point. Fig. 7.1 shows how this objective function evolves with change of α_1 and α_2 .

These maps show that for each confining pressure, there is a zone in α_1 - α_2 space producing relatively good fits (low objective function values) and potentially hosting a single global minimum. The location of this 'optimal zone' varies for each confining

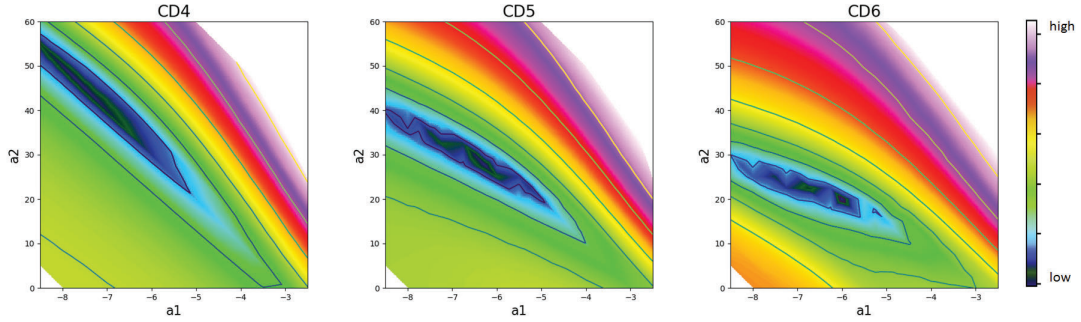


Figure 7.1: Map of the objective function in α_1 - α_2 space for CD4-6 of Noto mudstone. Blue color represents region of low cost. Interpolated via radial basis function.

pressure. The right columns of Fig. 7.2, like Fig. 7.1, show the evolution of this zone as a function of time/axial strain. It seems to be rotating over time, but the location of the global minimum remains surprisingly steady.

This sensitivity analysis also reveals that the valid ranges of α_1 and α_2 to get meaningful numerical results are quite narrow. For extreme values the simulation behaves in obviously incorrect ways, e.g. by dropping porosity all the way to zero, or never entering plasticity, and the corresponding zones on the maps have been cropped out (appearing as white areas).

7.3 Correlating simulation response to objective function

It is interesting to see if any of this behaviour could be captured directly in the numerical results themselves, in order to lessen the reliance on expensive experimental data. REDBACK has the ability to output various physical properties at each timestep. A non-exhaustive list is provided in Table 7.1. Note that unlike the cost function, which is a comparison of the simulation stress and strain to that of experiment data, the post-processors are generated purely based on the simulation itself.

Fig. 7.2 and Fig. 7.3 show two post-processors evolving over time, seemingly moving in sync with the objective function. Similar correlations of this sort can be observed in a broad range of post-processors, and across all three tested confining pressures, with the best correlations in the centre block, rather than average or extreme values.

The Q_{mech} post-processor tracks the activation enthalpy at the core of the model used in this work. Comparing this post-processor against the objective function (Fig. 7.2), the zone of good fit in the objective function seems to correspond to a narrow range of values of Q_{mech} .

Figures 7.3 and 7.4 shows the post-processor most closely matching the objective

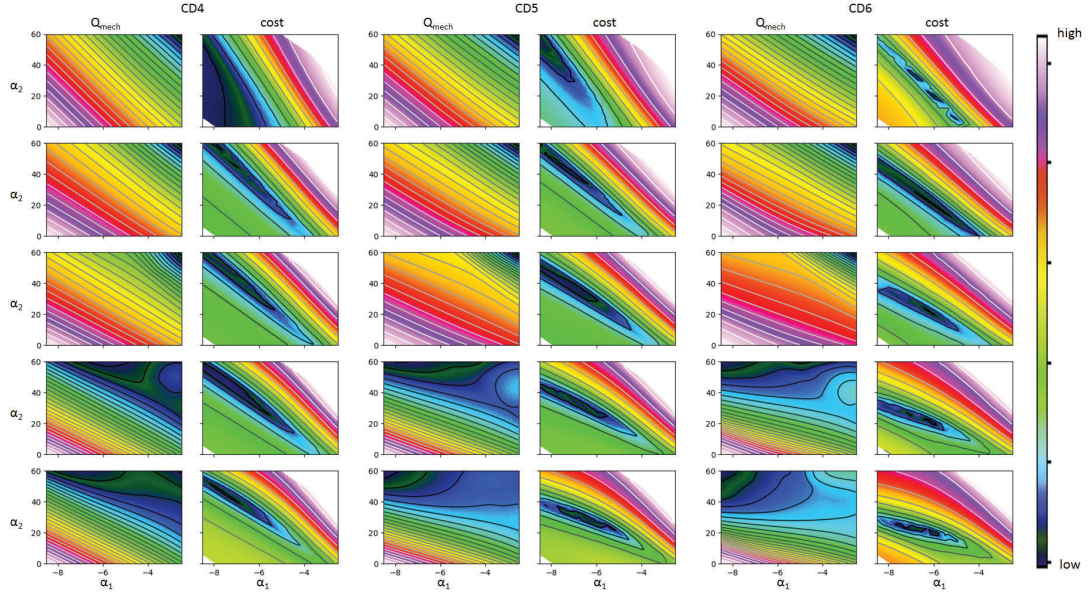


Figure 7.2: Evolution of the Q_{mech} post-processor and cost function (right) over time, from start of plasticity to end of experiment. The Q_{mech} data is taken from the center block. Blue represents low values, red represents high values, white represents omitted areas.

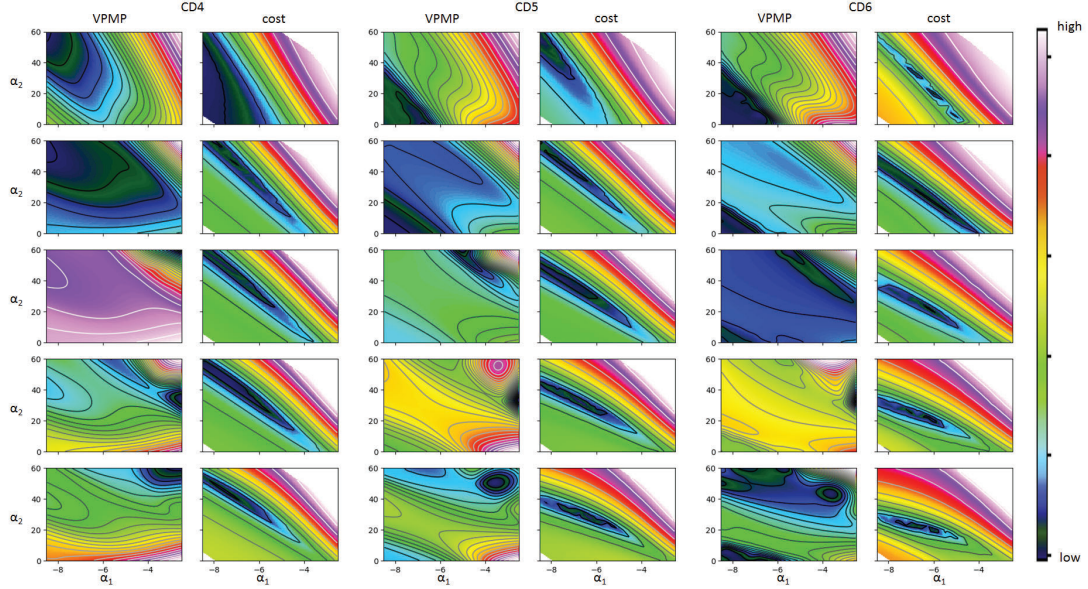


Figure 7.3: Evolution of the volumetric-plastic-mechanical-power post-processor (left) and objective function (right) over time, from the start of plasticity to end of experiment. The post-processor data is taken from the center block. Blue represents low values, red represents high values, white represents omitted areas.

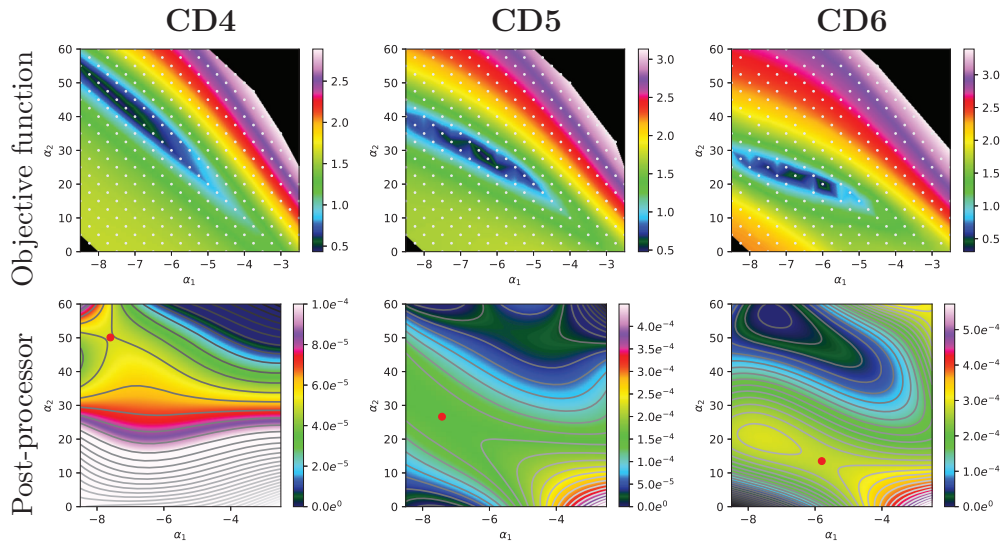


Figure 7.4: Sensitivity analysis in (α_1, α_2) parameter space for mudstone experiments CD4-6. The top row displays the value of the objective function interpolated from 313 simulations (white dots), showing a localised zone of good fits (low values). The bottom row shows the corresponding values of a post-processor computing the volumetric component of the plastic mechanical work at the center of the sample. The red dot shows the location of identified saddle points. Note that some colorbars were capped to exclude extreme values and better illustrate the patterns.

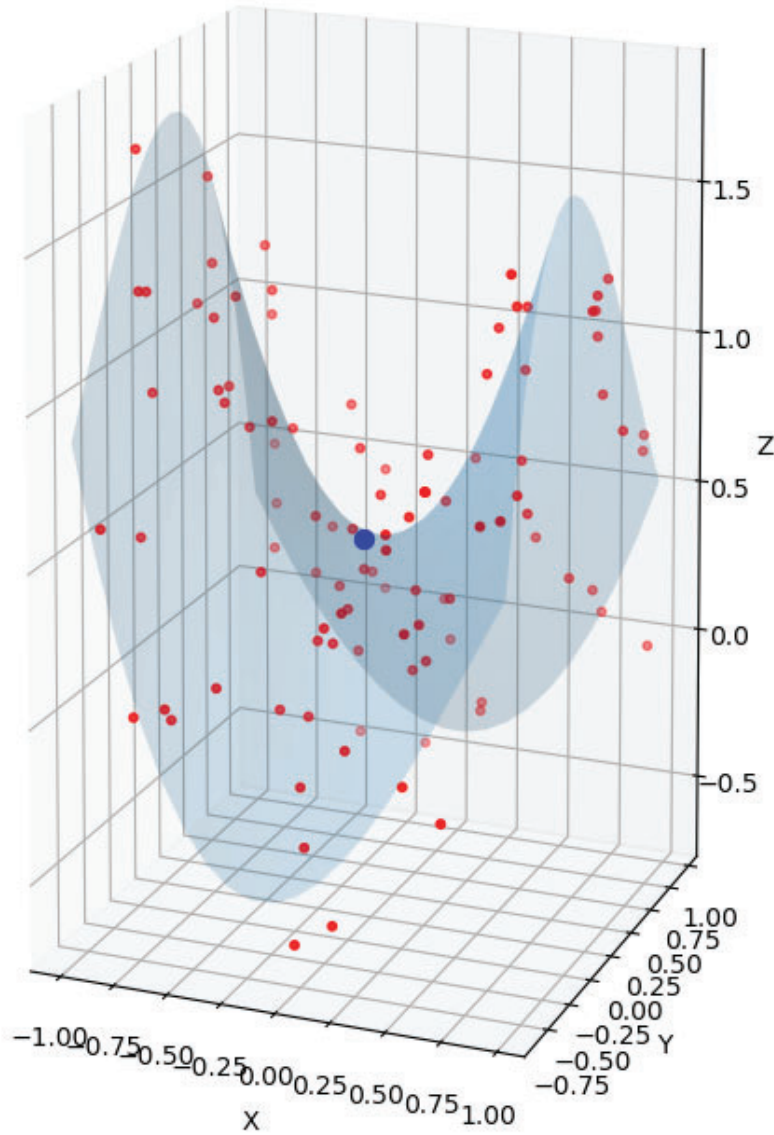


Figure 7.5: 3D plot of the process for finding a saddle point in α_1 - α_2 space, on a synthetic function $h(x, y) = x^2 - y^2$ to illustrate the functionality. Red dots are sampled from $h(x, y)$ with added noise. The light blue surface is the fitted polynomial $f(x, y)$, and the large dark blue dot is the found saddle point. Despite heavy noise, the polynomial tracks the underlying function closely, and the saddle point, found at $[-0.030, -0.008]$, is close to the analytical solution of $[0, 0]$.

function. It seems to consistently display a saddle point very close to the cost minima. Examining Fig. 7.3 it is possible to see that the strong match does not just happen at the end, instead the cost function and post-processor evolve in a synchronised manner throughout the experiment.

This *volumetric_plastic_mech_power* post-processor tracks the volumetric component of the plastic mechanical power in the center block. It is calculated by taking the product of the mean stress and plastic volumetric strain rate, two separate post-processors. When the mean stress and plastic volumetric strain rate maps are plotted separately, a 'ridge' is visible in different orientations. When multiplied, these ridges intersect to form a saddle point. The fact that the volumetric component offers a strong signal makes sense in the context of the plasticity model, which was designed to model pore collapse at high confinement.

7.4 Determining the saddle point in α_1 - α_2 space

To aid in future analyses, a routine has been implemented in Pathfinder for extracting the saddle point from a post-processor map.

As the (α_1, α_2) space is discretised, and the resolution is imperfect due to numerical precision, derivatives of this space contains a small but non-negligible noise component, making it difficult to track characteristic points directly. Instead, the routine first fits a 3rd-order polynomial $f(\alpha_1, \alpha_2)$ to the data. It then finds the saddle point of this (smooth) function, using a numerical approximation of the second partial derivative test. Fig. 7.5 highlights the localisation of the saddle point on a synthetic test function $h(x, y) = x^2 - y^2$ with added random noise of amplitude 1, showing that it is robust even when facing large amounts of noise.

7.4.1 Second partial derivative test

Since $f(\alpha_1, \alpha_2)$ is a 3rd-order polynomial, it is real, differentiable, and second partial derivatives exist. This means that the saddle point can be found via the second partial derivative test (Stewart, 2004). The test is as follows:

Defining H as the Hessian matrix of $f(\alpha_1, \alpha_2)$:

$$H(\alpha_1, \alpha_2) = \begin{bmatrix} f_{\alpha_1\alpha_1}(\alpha_1, \alpha_2) & f_{\alpha_1\alpha_2}(\alpha_1, \alpha_2) \\ f_{\alpha_1\alpha_2}(\alpha_1, \alpha_2) & f_{\alpha_2\alpha_2}(\alpha_1, \alpha_2) \end{bmatrix} \quad (7.1)$$

where the subscripts indicate derivatives of the function (e.g. $f_{\alpha_1\alpha_1} = \frac{\partial^2 f}{\partial \alpha_1 \partial \alpha_1}$).

Let D be the determinant of $H(\alpha_1, \alpha_2)$:

$$\begin{aligned} D(\alpha_1, \alpha_2) &= \text{Det}(H(\alpha_1, \alpha_2)) \\ &= f_{\alpha_1\alpha_1}(\alpha_1, \alpha_2)f_{\alpha_2\alpha_2}(\alpha_1, \alpha_2) - (f_{\alpha_1\alpha_2}(\alpha_1, \alpha_2))^2 \end{aligned} \quad (7.2)$$

For critical point (a, b) where $f_{\alpha_1}(a, b) = 0$ and $f_{\alpha_2}(a, b) = 0$,

1. If $D(a, b) < 0$ then (a, b) is a saddle point.
2. If $D(a, b) = 0$ then (a, b) is a saddle point, minima, or maxima.
3. Otherwise, (a, b) is not a saddle point.

7.4.2 Numerical approximation

Implementing the second derivative test above requires finding the critical points of the function. This means either analytically solving for its derivative or numerically solving for its roots. It is simpler to implement instead the following test:

1. Calculate a 2D matrix of values for the function in the region of interest.
2. For each point, calculate whether it is greater than each of its eight neighbours. Output 1 if greater, -1 otherwise.
3. Go clockwise through the eight neighbours, count the number of sign changes in the output of Step 2.
4. It is a saddle point if there are at least 4 sign changes.

Post-processor	Description
<i>lewis_number</i>	Lewis number, starting from value defined in input file.
<i>porosity</i>	Porosity, starting from ϕ_0 defined in input file.
<i>Qmech</i>	The constitutive term Q_{mech} as defined in Eq. 2.8.
<i>pore_pressure</i>	Normalized excess pore pressure.
<i>temp</i>	Normalized temperature.
<i>mises_stress</i>	deviatoric stress.
<i>mises_strain</i>	the equivalent plastic strain.
<i>mises_strain_rate</i>	time derivative of above.
<i>mean_stress</i>	volumetric mean stress.
<i>plastic_volumetric_strain</i>	plastic portion of volumetric strain.
<i>plastic_volumetric_strain_rate</i>	time derivative of above.
<i>deviatoric_pmw</i>	Deviatoric component of plastic mechanical work. = $mises_stress * mises_strain$
<i>volumetric_pmw</i>	Volumetric component of plastic mechanical work. = $mean_stress * plastic_volumetric_strain$
<i>plastic_mech_work</i>	Total plastic mechanical work. = $deviatoric_pmw + volumetric_pmw$
<i>deviatoric_pmp</i>	Deviatoric component of plastic mechanical power. = $mises_stress * mises_strain_rate$
<i>volumetric_pmp</i>	Volumetric component of plastic mechanical power. = $mean_stress * plastic_volumetric_strain_rate$
<i>plastic_mech_power</i>	Total plastic mechanical power. = $deviatoric_pmp + volumetric_pmp$
<i>top_avg_stress_yy</i>	A measure of the deviatoric stress, averaged over the top face of the rock sample.

Table 7.1: Partial List of post-processors in REDBACK. Each post-processor except for *top_avg_stress_yy* is calculated in three locations: in the centre block, averaged over entire volume, and the extrema (min or max depending on context) of the entire volume.

Chapter 8

Discussion and conclusion

This study showcased a heuristic inversion workflow for calibrating a thermo-hydro-mechanical model based on elasto-visco-plasticity against triaxial experimental data. I demonstrated the ability of the underlying physical model to capture both the volumetric and deviatoric behaviours of rock deformation for two different cases, mudstone and sandstone (see Chapters 5 and 6), building on previous work which had showed promising results on mudstone for the deviatoric behaviour only (Poulet & Veveakis, 2016). The heuristic nature of the approach is an important component, both from numerical and theoretical reasons. Numerically, the multi-physical nature of the model obviously grows considerably the number of parameters that need to be inverted, which comes at an exponential computational cost in terms of simulations needed to parse the parameter space. As such, the breakdown of the inversion process in three separate stages, as described on Fig. 3.1, provides individual steps that are much more manageable computationally. The numerical argument, however, does not represent the major reason for this breakdown, which is even more important for theoretical reasons. Those stages represent indeed a much better way for theoretical modellers to understand the behaviour of their physical model in terms of parameter sensitivity, compared with a single-step optimisation approach. In practice, the data driven approach presented here provided a better understanding of the flow law description used (Eq. 2.8) and led to the discovery of a potentially game-changing property of the model with the presence of a saddle point (see Fig. 7.3).

The time and cost of running laboratory experiments are important factors to take into consideration when characterising a rock behaviour and using numerical simulations to minimise those costs is certainly very appealing. The potential presence of a saddle point in the volumetric component of the plastic mechanical power, as shown in Sec. 7.3, is therefore a critical outcome of this study as it could help reduce the number of laboratory experiments needed to calibrate this physical model. The

theoretical study of the physical reasons for this behaviour clearly falls outside the scope of this work, but it is important to note the role of a data-driven analysis to infer information about a theoretical model to help its development. This reinforces the significance of taking a heuristic approach and highlights the need not to de-correlate too quickly the complementary physically-driven and data-driven approaches, as they both strongly benefit from a tight and simultaneous interaction.

It is also worth mentioning some other conclusions drawn from this calibration exercise regarding the concept of the yield envelope, as well as the important physical roles of temperature, pressure and rate sensitivity of materials.

The distinction between an experimentally obtained yield envelope at the sample scale and the yield surface required at the smaller scale for equivalent finite element simulations has always been an admitted concept in theory. In this contribution, I considered the possibility to use a scaled-down version of the experimental curves (see Subsec. 2.1.4) and showed satisfactory modelling results which justify further investigations of this approach. Once again, the theoretical justification of this method falls outside the scope of this work, but the results highlight the important role of numerical investigations to help infer theoretical knowledge on constitutive relationships.

The results obtained in Chapters 5 and 6 demonstrate as well the temperature, pressure and rate dependency of the materials tested, showing that it is possible to capture relatively well already the physical reasons behind the puzzling hardening/weakening evolution with confining pressure. While Sec. 2 presented theoretical reasons to take into account those mechanisms, the interpretation of the results justifies those considerations.

Most models treat triaxial experiments as isothermal, which is not necessarily justified a priori as discussed in Subsec. 2.1.1. From the results obtained I can now illustrate more precisely the effect of considering temperature variations, at least in terms of overall impact, since its effects are feeding back on pore pressure and stress through the various feedbacks considered in the system of equations (Eq. 2.8). Fig. 8.1 shows the thermal weakening of the model and the sensitivity of the Gruntfest number Gr , encompassing the micro-structural shear heating effects, on the stress-strain response of mudstone at 1.5 MPa confinement for instance. There is a slight weakening occurring when increasing Gr by a factor 5, while the maximum temperature changes (at the centre of the virtual rock sample) remain below a maximum of 0.3°C. These minor temperature variations within the sample would remain barely noticeable from the outside using a recent thermal infra-red camera, which shows the important effects of even minor temperature changes. Note as well the temperature feedback on the mechanical behaviour through the temperature dependency of the mechanical flow law and the Arrhenius parameter Ar (Eq. 2.8), with a sensitivity analysis for the same

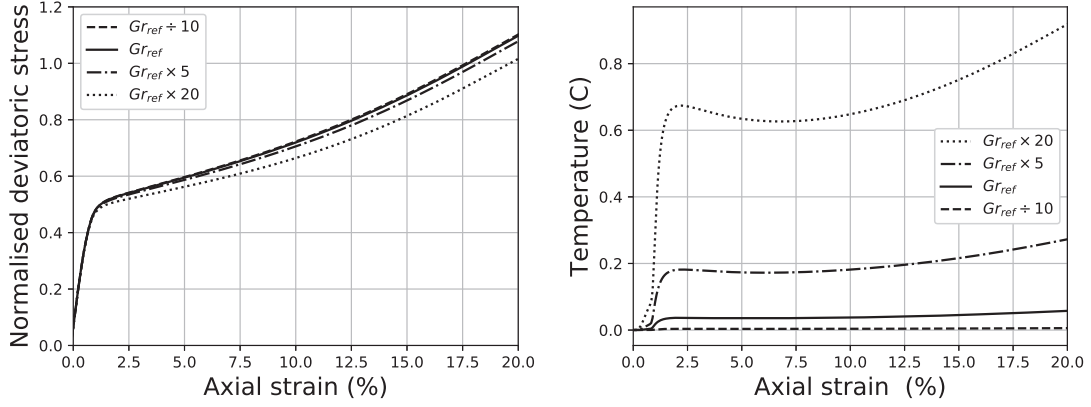


Figure 8.1: Sensitivity analysis on Gruntfest number Gr , showing noticeable temperature weakening on the stress-strain curves (left) for corresponding temperature values (right) not exceeding 1°C at the centre of the 3D block.

simulation shown in Fig. 8.2. The effects on the mechanical response are even more drastic, with temperature changes yet remaining once again below noticeable values from the outside.

Similar to temperature, pore pressure effects also play an important role in the results obtained and highlight the range of values required for the Lewis number Le for the pressure sensitivity of the flow law to become relevant. While the definition of Le from Eq. (2.4a) only accounts for Darcy flow in terms of mass diffusivity, the higher values obtained through the inversion - up to 5 orders of magnitude for sandstone for instance - point to the fact that other mechanisms are at play and should be accounted for in the physical model. This finding highlights once again the importance of the numerical approach to help derive the physical model, and to allow flexible bounds for poorly constrained numbers (like Le) as a good way to infer new directions for the theoretical model development. For instance, Sari (2019) proposed recently a new formulation of the mechanical flow law accounting for the mass diffusivity of a weaker solid phase resulting from grain de-bonding and cement breakage, which would indeed translate in the current model as much larger values of Le .

Finally, the rate sensitivity built into the model has already been demonstrated (Poulet & Veveakis, 2016) and proved as well to play a role in the calibration studies presented here. Considering creep brings more focus on the impact of the loading rates used to equilibrate the laboratory experiments at high confinements, especially as reduced yield envelopes are also in play. This raises the interesting question whether some creep had actually started in places, at the microstructural level, for the experiments at highest confinements. This question can only be answered in the laboratory but points again at the surprising impact of the data-driven numerical approach be-

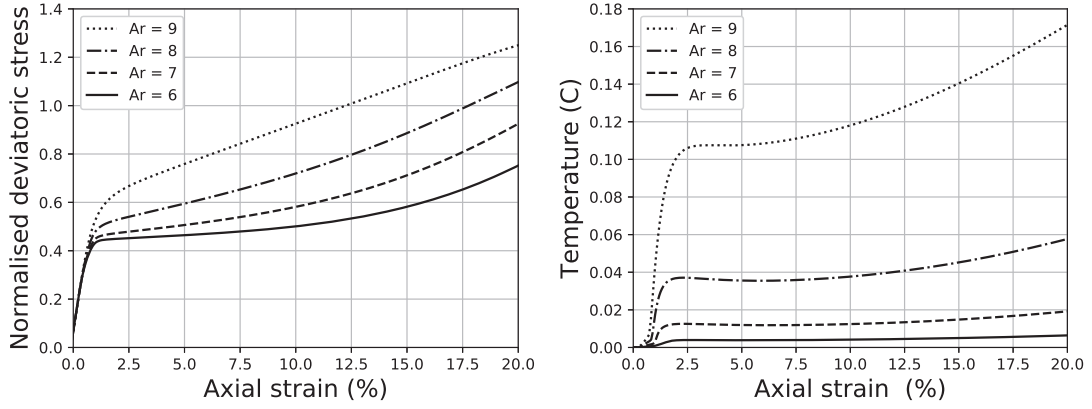


Figure 8.2: Sensitivity analysis on Arrhenius number Ar , showing extremely different mechanical responses on the stress-strain curves (left) for corresponding temperature values (right) not exceeding 0.2°C at the centre of the 3D block.

yond its originally intended scope.

The derived set of parameters are not necessarily unique, but they closely fit the experimental observations of rock behaviour, and the presence of a saddle point satisfies heuristics regarding the interaction between multiple competing processes. Ultimately there is no way to ‘ensure’ a match with physical reality, but the close matches obtained warrant some validity of the approach via Occam’s Razor, and warrant further investigations into the proposed model. Like all models, it is a simplification of reality, but it is one that has proven useful.

Going forward, improvement could come from several directions: insight could be obtained through calibrating the model to a wider range of experiments, covering more rock types and broader range of experiment conditions. The model could be expanded to include considerations such as sample anisotropy and clay swelling. Advancing the theoretical underpinnings for the identified constitutive parameters could lead to elimination of some of the free parameters and improve predictive power.

In conclusion, this study demonstrated the importance of linking theoretical and numerical investigations as both approaches are so complementary in the context of multiphysics that they cannot satisfactorily be tackled independently. The workflow presented here provides a practical step towards this goal and showed the impact of combining physically-driven and data-driven approaches. This approach is of particular interest for applications including landslides, subduction zones, nuclear waste disposal, or any other geological deformation focusing on plasticity with multiphysical feedbacks. The formulation of a physical model accounting directly for temperature and pressure evolution could open the door to possible extrapolations of existing laboratory results beyond the conditions previously tested (high temperature, high

pressure, geological strain rates) and such novel theories will certainly require an even tighter experimental-theoretical-numerical integration.

References

- Abramson, D., Enticott, C., & Altinas, I. (2008, Nov). Nimrod/k: Towards massively parallel dynamic grid workflows. In *Sc '08: Proceedings of the 2008 acm/ieee conference on supercomputing* (p. 1-11). doi: 10.1109/SC.2008.5215726
- Babbage, C., & Baudouin, C. (2009). *Passages from the life of a philosopher*. Read Books. Retrieved from https://books.google.com.au/books?id=b7_Lz0QMBdWC
- Broomhead, D. S., & Lowe, D. (1988). *Radial basis functions, multi-variable functional interpolation and adaptive networks* (Tech. Rep.). Royal Signals and Radar Establishment Malvern (United Kingdom).
- Broyden, C. G. (1970, 03). The Convergence of a Class of Double-rank Minimization Algorithms 1. General Considerations. *IMA Journal of Applied Mathematics*, 6(1), 76-90. Retrieved from <https://doi.org/10.1093/imamat/6.1.76> doi: 10.1093/imamat/6.1.76
- David, C., Wong, T.-F., Zhu, W., & Zhang, J. (1994). Laboratory measurement of compaction-induced permeability change in porous rocks: Implications for the generation and maintenance of pore pressure excess in the crust. *Pure and Applied Geophysics*, 143(1-3), 425–456.
- Deelman, E., Vahi, K., Juve, G., Rynge, M., Callaghan, S., Maechling, P. J., ... Wenger, K. (2015). Pegasus, a workflow management system for science automation. *Future Generation Computer Systems*, 46, 17 - 35. Retrieved from <http://www.sciencedirect.com/science/article/pii/S0167739X14002015> doi: <https://doi.org/10.1016/j.future.2014.10.008>
- Gaston, D., Newman, C., Hansen, G., & Lebrun-Grandi, D. (2009, Oct). Moose: A parallel computational framework for coupled systems of nonlinear equations. *Nuclear Engineering and Design*, 239(10), 1768–1778. doi: 10.1016/j.nucengdes.2009.05.021
- Gerolymatou, E. (2017). *Induced and inherent anisotropy in rock mass* (Unpublished doctoral dissertation). Fakultät für Bauingenieur-, Geo- und Umweltwissenschaften (BGU), Karlsruher Institut für Technologie. (Habilitation)
- git(1) manual page*. (2019). Retrieved from <https://git-scm.com/docs/git.html> ([Online; accessed 8-March-2019])

- Holland, J. H. (1992, July). Genetic algorithms. *Scientific American*.
- Kennedy, J., & Eberhart, R. (1995, Nov). Particle swarm optimization. In *Proceedings of icnn'95 - international conference on neural networks* (Vol. 4, p. 1942-1948 vol.4). doi: 10.1109/ICNN.1995.488968
- Liew, C. S., Atkinson, M. P., Galea, M., Ang, T. F., Martin, P., & Hemert, J. I. V. (2016, December). Scientific workflows: Moving across paradigms. *ACM Comput. Surv.*, 49(4), 66:1–66:39. Retrieved from <http://doi.acm.org/10.1145/3012429> doi: 10.1145/3012429
- Lin, J., Sari, M., Poulet, T., & Veveakis, M. (2017). An inversion framework for numerical modelling of pore collapse in soft porous rocks. In E. Papamichos, P. Papanastasiou, E. Pasternak, & A. Dyskin (Eds.), *Bifurcation and degradation of geomaterials with engineering applications: Proceedings of the 11th international workshop on bifurcation and degradation in geomaterials dedicated to hans muhlhaus, limassol, cyprus, 21-25 may 2017* (pp. 319–325). Cham: Springer International Publishing. doi: 10.1007/978-3-319-56397-8_40
- Ludäscher, B., Altintas, I., Berkley, C., Higgins, D., Jaeger, E., Jones, M., . . . Zhao, Y. (2006, August). Scientific workflow management and the kepler system: Research articles. *Concurr. Comput. : Pract. Exper.*, 18(10), 1039–1065. Retrieved from <http://dx.doi.org/10.1002/cpe.v18:10> doi: 10.1002/cpe.v18:10
- Maekawa, H., & Miyakita, K. (1983). Mechanical properties of diatomaceous soft rock. *Proceedings of the Japan Society of Civil Engineers*, 1983(334), 135-143.
- Mielke, A. (2006). Multifield problems in solid and fluid mechanics. In (pp. 399–428). Springer Berlin / Heidelberg. doi: 10.1007/978-3-540-34961-7_12
- Nelder, J. A., & Mead, R. (1965, 01). A Simplex Method for Function Minimization. *The Computer Journal*, 7(4), 308-313. Retrieved from <https://doi.org/10.1093/comjnl/7.4.308> doi: 10.1093/comjnl/7.4.308
- Nguyen-Tuan, L., Lahmer, T., Datcheva, M., Stoimenova, E., & Schanz, T. (2016). A novel parameter identification approach for buffer elements involving complex coupled thermo-hydro-mechanical analyses. *Computers and Geotechnics*, 76, 23 - 32. doi: <https://doi.org/10.1016/j.compgeo.2016.02.005>
- Oka, F., Kimoto, S., Higo, Y., Ohta, H., Sanagawa, T., & Kodaka, T. (2011). An elasto-viscoplastic model for diatomaceous mudstone and numerical simulation of compaction bands. *International Journal for Numerical and Analytical Methods in Geomechanics*, 35(2), 244–263.
- Parker, S. (2003). *Mcgraw-hill dictionary of scientific and technical terms*. McGraw-Hill Education. Retrieved from <https://books.google.com.au/books?id=xOPz05HVFfEC>
- Perzyna, P. (1966). Fundamental problems in viscoplasticity. *Advances in Applied Mechanics*, 9, 244 - 377. doi: [http://dx.doi.org/10.1016/S0065-2156\(08\)70009-7](http://dx.doi.org/10.1016/S0065-2156(08)70009-7)

- Poulet, T., Paesold, M., & Veveakis, E. (2017). Multi-physics modelling of fault mechanics using redback - a parallel open-source simulator for tightly coupled problems. *Rock Mechanics and Rock Engineering*, 50(3), 733–749. doi: 10.1007/s00603-016-0927-y
- Poulet, T., & Veveakis, M. (2016). A viscoplastic approach for pore collapse in saturated soft rocks using redback: An open-source parallel simulator for rock mechanics with dissipative feedbacks. *Computers and Geotechnics*, 74, 211 - 221. Retrieved from <http://www.sciencedirect.com/science/article/pii/S0266352X15002785> doi: <https://doi.org/10.1016/j.compgeo.2015.12.015>
- Robbins, H., & Monroe, S. (1951). A stochastic approximation method. *The Annals of Mathematical Statistics*, 22(3), 400–407. Retrieved from <http://www.jstor.org/stable/2236626>
- Sari, M. (2019). *A multi-physics plasticity theory for porous sedimentary rocks* (Unpublished doctoral dissertation). UNSW Minerals and Energy Resources Engineering, Sydney, Australia. ((under review))
- Sari, M., Alevizos, S., Poulet, T., Lin, J., & Veveakis, E. (2019, May). *A temperature- and pressure-sensitive visco-plasticity theory based on interface mechanisms for sedimentary rocks*. EarthArXiv. Retrieved from eartharxiv.org/g68uw doi: 10.31223/osf.io/g68uw
- scipy.interpolate.rbf*. (2019). Retrieved from <https://docs.scipy.org/doc/scipy/reference/generated/scipy.interpolate.Rbf.html> ([Online; accessed 8-March-2019])
- Stewart, J. (2004). *Multivariable calculus: Concepts and contexts: Concepts and contexts*. Thomson Brooks/Cole. Retrieved from <https://books.google.com.au/books?id=eNHhKxXCJaEC>
- Tembe, S., Vajdova, V., Baud, P., Zhu, W., & Wong, T.-F. (2007). A new methodology to delineate the compactive yield cap of two porous sandstones under undrained condition. *Mechanics of materials*, 39(5), 513–523.
- tisimst. (2019). *Particle swarm optimization (pso) with constraint support*. Retrieved from <https://github.com/tisimst/pyswarm> ([Online; accessed 8-March-2019])
- Wijns, C., Poulet, T., Boschetti, F., Dyt, C., & Griffiths, C. (2004). Interactive inverse methodology applied to stratigraphic forward modelling. *Geological Society Special Publication*, 239, 147-156. (cited By (since 1996) 6)
- Wolpert, D. H., & Macready, W. G. (1997, April). No free lunch theorems for optimization. *IEEE Transactions on Evolutionary Computation*, 1(1), 67-82. doi: 10.1109/4235.585893

- Wolstencroft, K., Haines, R., Fellows, D., Williams, A., Withers, D., Owen, S., ... Goble, C. (2013, 05). The Taverna workflow suite: designing and executing workflows of Web Services on the desktop, web or in the cloud. *Nucleic Acids Research*, 41(W1), W557-W561. Retrieved from <https://doi.org/10.1093/nar/gkt328>
doi: 10.1093/nar/gkt328
- Wong, T., & Baud, P. (1999). Mechanical compaction of porous sandstone. *Oil & Gas Science and Technology*, 54(6), 715–727.
- Wong, T.-F., David, C., & Zhu, W. (1997). The transition from brittle faulting to cataclastic flow in porous sandstones: Mechanical deformation. *Journal of Geophysical Research: Solid Earth*, 102(B2), 3009–3025.
- Wu, L., Liu, S., Wu, Y., & Wang, C. (2006). Precursors for rock fracturing and failure part i: Irr image abnormalities. *International Journal of Rock Mechanics and Mining Sciences*, 43(3), 473 - 482. doi: <https://doi.org/10.1016/j.ijrmms.2005.09.002>
- Zhu, W., Montesi, L., & Wong, T.-F. (2008). Characterizing the permeability-porosity relationship during compactive cataclastic flow. In *The 42nd us rock mechanics symposium (usrms)*.
- Zhu, W., & Wong, T.-F. (1997). The transition from brittle faulting to cataclastic flow: Permeability evolution. *Journal of Geophysical Research: Solid Earth*, 102(B2), 3027-3041. Retrieved from <https://agupubs.onlinelibrary.wiley.com/doi/abs/10.1029/96JB03282>
doi: 10.1029/96JB03282